nature cities

Supplementary information https://doi.org/10.1038/s44284-024-00184-9

Exacerbated heat stress induced by urban browning in the Global South

In the format provided by the authors and unedited

Table of contents

A. Supplementary Notes

<u>Note S1</u>: *Validation of urban HI estimates and associated trends, as well as the potential impacts of urban HI estimation errors on calculating K_{HI} and β_{HI}*

We evaluated the accuracy of the generated urban heat index (HI) dataset by conducting cross-validations with *in-situ* observations, concentrating on both absolute values and temporal trends (K_{HI}; Supplementary Figs. 20 to 23). This validation process involved calculating four error metrics, i.e., correlation coefficient (R), root mean square error (RMSE), mean absolute error (MAE), and bias, between the observed and estimated urban HI values as well as their trends.

Regarding absolute urban HI, we used 80% of *in-situ* observation records for training random forest (RF) models and the remaining 20% for validation. This method yielded 3273 and 2765 observation records for daytime and nighttime validation, respectively. Our assessments revealed high accuracy of absolute urban HI estimates across Global South cities, with an R value of 0.98 for both daytime and nighttime, an RMSE value of 1.11 °C for daytime and 0.86 °C for nighttime, an MAE value of 0.82 °C for daytime and 0.62 °C for nighttime, and a bias of −0.006 °C for daytime and 0.007 °C for nighttime (Supplementary Fig. 20a,b). Across various sub-continents, our accuracy assessments revealed the biases of −0.003 °C for daytime and −0.006 °C for nighttime in Asian cities, −0.04 °C for daytime and 0.04 °C for nighttime in Latin American cities, and 0.03 °C for daytime and 0.07 °C for nighttime in African cities (Supplementary Fig. 22). These biases only account for less than 1% of the observed urban HI values in Asian, Latin American, and African cities, respectively.

Regarding K_{HI}, we employed urban stations with complete records across all years for validation, totaling 553 and 366 stations for daytime and nighttime validation, respectively (Supplementary Fig. 20c,d). We compared the observed urban K_{HI} derived from ground-based measurements with predicted values from model estimations at corresponding pixel locations of urban stations. Our evaluations indicated slightly lower accuracy of K_{HI} compared to the absolute urban HI, with an R value of 0.82 for daytime and 0.74 for nighttime, an RMSE value of 0.58 °C/decade for daytime and 0.45 °C/decade for nighttime, an MAE value of 0.40 °C/decade for daytime and 0.32 °C/decade for nighttime, and a bias of −0.12 °C/decade for daytime and −0.10 °C/decade for nighttime. Concerning sub-continents, our assessments revealed biases in K_{HI} of −0.16 °C/decade for daytime and −0.15 °C/decade for nighttime in Asian cities, −0.04 °C/decade for daytime and 0.12 °C/decade for nighttime in African cities, and −0.02 °C/decade for daytime and −0.01 °C/decade for nighttime in Latin American cities (Supplementary Fig. 23). These biases represent approximately 26%, 24%, and 5% of the observed urban K_{HI} in Asian, African, and Latin American cities, respectively. The relatively larger estimation biases observed in Asian and African cities are likely attributable to the more rapid urbanization in these regions over recent decades[1], which may result in disturbances to their ground-based observations in urban areas, such as through the relocation of monitoring stations[2].

We further investigated the impacts of urban HI estimation error by re-examining the K_{HI} and browning-induced K_{HI} (β_{HI}) using an error injection strategy[3]. Specifically, we first generated a random error field with 1-km resolution based on the absolute MAE of urban HI as mentioned above (i.e., 0.82 °C for daytime and 0.62 °C for nighttime), with the generated errors normally distributed with a mean of 0.0 °C and with standard deviations of 0.82 °C and 0.62 °C for daytime and nighttime, respectively. Secondly, we re-produced a new urban HI dataset by superimposing this 1-km resolution random error field on the original 1-km urban HI dataset. Finally, we re-examined the K_{HI} and β_{HI} across Global South cities using this newly generated urban HI dataset, and compared them with the original results (Supplementary Fig. 28). Our evaluations show that the K_{HI} quantified based on this error-perturbed HI dataset is 0.43 ± 0.01 °C/decade during the day and 0.39 ± 0.01 °C/decade at night (Supplementary Fig. 28a,c), deviating from the original results of < 0.01 °C/decade. Additionally, the β_{HI} estimated based on these error-perturbed HI values is 0.021 ± 0.002 °C/decade for both daytime and nighttime, also on well par with the original estimates (Supplementary Fig. 28b,d). These assessments strongly support the reliability of the generated urban HI dataset and the main findings of this study.

In practice, these significantly reduced estimation errors at the global scale compared to those encountered at the per-pixel scale can be elucidated through the Bessel formula[4,5] ($\frac{\delta}{\sqrt{n-1}}$, with n denoting the sample number and δ representing the error for an individual pixel). This formula suggests that the impact of individual sample errors could be mitigated through extensive averaging processes. For our current study, we first averaged the HI of all available urban pixels for a city to quantify the city-scale HI trend. Then, we aggregated these city-scale trends into global or regional composites to reveal large-scale spatial patterns. These multi-averaging processes could help dampen the impact of estimation error on HI trends at larger scales. Studies that quantify global warming rates also evidence the significantly reduced estimation error by multi-averaging processes. For instance, the global surface air temperature has shown an average increase of around 0.11 °C/decade since 1850 (ref. 6). While the error associated with ground-based surface air temperatures from weather stations is also of a comparable magnitude (i.e., around 0.1 °C), this does not imply that the influence of site observation error would exert a similar impact on the quantification of global warming rates.

Note S2: ***Impacts from the limited number of urban stations on the accuracy of generated 1-km resolution urban HI dataset***

This study integrated *in-situ* measurements from > 9600 weather stations sourced from the HadISD dataset to generate urban HI datasets at 1-km resolution for Global South cities. One might raise concerns about the relatively sparse distribution of our incorporated weather stations within these cities (Supplementary Fig. 1b), which may introduce potential uncertainties into the estimation of urban HI due to high urban heterogeneity. To address this, we performed an additional sensitivity analysis by incorporating data from the Berkeley Earth dataset. Unlike HadISD, Berkeley Earth offers a more extensive collection of ground-based observations globally (> 47,000 stations), with 3304 stations located on urban surfaces in the Global South – 2.5 times the number in HadISD[7] (Supplementary Fig. 1b). However, the Berkeley Earth dataset solely provides *in-situ* surface air temperature (SAT) measurements and lacks humidity data, precluding a direct assessment of the impact of urban station density on the calculation of K_{HI}. Consequently, we first generated 1-km resolution urban SAT datasets across Global South cities using both the Berkeley Earth and HadISD datasets, and then compared the urban warming rates (K_{SAT}) derived from these two sources.

Our evaluations demonstrate that the K_{SAT} derived from both the Berkeley Earth and HadISD datasets exhibits remarkably similar spatial patterns and values across Global South cities (Supplementary Fig. 24). The numerical differences between them are only 0.01 °C/decade during the day (0.31 °C/decade for Berkeley Earth and 0.32 °C/decade for HadISD) and 0.03 °C/decade at night (0.31 °C/decade for Berkeley Earth and 0.28 °C/decade for HadISD). This close alignment could be attributed to the relatively uniform distribution of weather stations provided by the HadISD dataset across all geographic regions in the Global South, thereby ensuring the accuracy of the generated 1-km resolution urban HI time-series data.

Note S3: ***Possible uncertainties related to the choice of urban heat stress indices***

In this study, we utilized the widely recognized Heat Index (HI; equations 1 and 2) as a metric to characterize the trends in heat stress across cities in the Global South. One may argue that the choice of heat stress metric could impact the main findings. To address this concern, we conducted a sensitivity analysis by introducing the Wet-Bulb Globe Temperature in shade conditions at stable wind (i.e., indoor WBGT; equation 3; ref. 8), and the Humidex recognized by the Meteorological Service of Canada[9–12] (equation 4). Following a similar approach as with HI, we initially generated 1-km urban datasets for indoor WBGT and Humidex across Global South cities. Subsequently, we quantified their long-term trends (K_{WBGT} and K_{Humidex}) and the impacts of vegetation loss on these trends (β_{WBGT} and β_{Humidex}), and compared them with those obtained from our primary metric (i.e., HI).

Our sensitivity analysis reveals that alternative indices (i.e., HI, indoor WBGT, and Humidex) yield consistent overall spatial patterns for both urban heat stress trends and browning-induced impacts (Supplementary Figs. 3 and 25). Regarding magnitudes, daytime and nighttime K_{WBGT} are 0.18 °C/decade and 0.25 °C/decade, respectively (Supplementary Fig. 3e,f), while for K_{Humidex}, these values translate to 0.36 °C/decade during the day and 0.46 °C/decade at night (Supplementary Fig. 3g,h). Moreover, the daytime and nighttime β_{WBGT} are 0.009 °C/decade and 0.011 °C/decade, respectively, and those of β_{Humidex} are 0.017 °C/decade and 0.019 °C/decade, respectively (Supplementary Fig. 29). The observed disparities across these three indices may stem from their varying sensitivities to air temperature (SAT) and humidity (RH). HI and Humidex, which place greater emphasis on air temperature and relatively less on humidity[13,14], exhibit more pronounced trends than WBGT (Supplementary Fig. 30).

Our current study did not utilize Humidex due to its dimensionless nature[15], limiting its comparability with other temperature and heat stress indices. Furthermore, the standard WBGT, rather than indoor WBGT, was not selected because its computation incorporates additional intricate meteorological parameters such as wind speed and radiation[16], which are challenging to obtain over urban landscapes from observations. We recommend practitioners carefully consider their research objectives and data accessibility when selecting heat stress metrics to ensure optimal decision-making and application.

Equation for calculating HI:

$$\begin{cases} \mathrm{HI} = \mathrm{A} + \mathrm{B} + \mathrm{C} - \mathrm{D} - \mathrm{E} - \mathrm{F} + \mathrm{G} + \mathrm{H} - \mathrm{I} \\ \mathrm{A} = -42.379 \\ \mathrm{B} = 2.04901523 \times \mathrm{SAT} \\ \mathrm{C} = 10.14333127 \times \mathrm{RH} \\ \mathrm{D} = 0.22475541 \times \mathrm{SAT} \times \mathrm{RH} \\ \mathrm{E} = 6.83783 \times 10^{-3} \times \mathrm{SAT}^2 \\ \mathrm{F} = 5.481717 \times 10^{-2} \times \mathrm{RH}^2 \\ \mathrm{G} = 1.22874 \times 10^{-3} \times \mathrm{SAT}^2 \times \mathrm{RH} \\ \mathrm{H} = 8.5282 \times 10^{-4} \times \mathrm{SAT} \times \mathrm{RH}^2 \\ \mathrm{I} = 1.99 \times 10^{-6} \times \mathrm{SAT}^2 \times \mathrm{RH}^2 \end{cases} \tag{1}$$

where SAT and RH denote surface air temperature (°F) and relative humidity (%), respectively. Adjustments were made according to various SAT and RH ranges[17]. When the average of HI and SAT values is less than 80 °F, we quantified HI using the following equation:

$$\mathrm{HI} = 0.5 \times [\mathrm{SAT} + 61 + [(\mathrm{SAT} - 68) \times 1.2] + (0.094 \times \mathrm{RH})] \tag{2}$$

Equation for calculating indoor WBGT:

$$\begin{cases} \mathrm{WBGT} = 0.7 \times T_{\mathrm{w}} + 0.3 \times \mathrm{SAT} \\ T_{\mathrm{w}} = \mathrm{A} + \mathrm{B} - \mathrm{C} + \mathrm{D} - \mathrm{E} \\ \mathrm{A} = \mathrm{SAT} \times \tan^{-1}[0.151977(\mathrm{RH} + 8.313659)^{1/2}] \\ \mathrm{B} = \tan^{-1}(\mathrm{SAT} + \mathrm{RH}) \\ \mathrm{C} = \tan^{-1}(\mathrm{RH} - 1.676331) \\ \mathrm{D} = 0.00391838(\mathrm{RH})^{3/2} \tan^{-1}(0.023101\mathrm{RH}) \\ \mathrm{E} = 4.686035 \end{cases} \quad (3)$$

where T_{w}, SAT, and RH denote wet bulb temperature (°C), surface air temperature (°C), and relative humidity (%), respectively.

Equation for calculating Humidex:

$$\mathrm{Humidex} = \mathrm{SAT} + 0.5555 \times (6.11 \times e^{5417.753 \times (\frac{1}{273.16} - \frac{1}{273.15 + T_{\mathrm{d}}})} - 10) \quad (4)$$

where T_{d} denotes dewpoint temperature (°C) and was quantified using SAT (°C), and RH (%).

Note S4: ***Country-level assessment of the inequality in β_{HI} across the Global South***

To reveal the inequality of urban heat stress trends induced by urban browning (β_{HI}), we conducted a country-level assessment of the Gini coefficient[10,18,19] of β_{HI} (termed Gini_β), as per equation (5):

$$\mathrm{Gini}_\beta = 1 - 2\int_0^1 L(\beta)\mathrm{d}\beta \tag{5}$$

where $L(\beta)$ represents the Lorenz curve of β_{HI}. For each country, we normalized the β_{HI} for all cities into the (0, 1) range and arranged them in the ascending order. The cumulative value of β_{HI} (0, 1) was then calculated, based on which the Lorenz curve of β_{HI} was represented as the graphical relationship between cumulative β_{HI} (0, 1) and the cumulative number of cities. Among different countries, larger Gini_β values suggest greater inequality in β_{HI}. Our analysis was limited to countries with at least ten cities to ensure statistical validity.

Our analysis reveals a positive correlation between country-level Gini_β and β_{HI} (Supplementary Fig. 31). Notably, cities in Ghana and Vietnam stand out with both larger β_{HI} (> 0.050 °C/decade; Fig. 13a,d) and higher Gini_β (> 0.40; Fig. 13b,e). Interestingly, we reveal a declining triangular relationship between Gini_β and GDP per capita across Global South countries (Fig. 13c,f). Specifically, Gini_β exhibits a wide range of values in economically disadvantaged countries (e.g., > 0.40 in Nigeria and Vietnam, < 0.25 in Pakistan and India). In contrast, its values remain in a lower range as economic status improves. Notably, countries like Nigeria, Colombia, Turkmenistan, and Chile exhibit higher Gini_β when compared with their peers of similar economic status (Fig. 13c,f). This result may indicate disproportional green space loss and a lack of planning and management, underscoring the urgency of drawing attention to these specific cases.

Note S5: ***Quantifying the increase in the number of ‘Danger’ days in Malaysian cities due to vegetation loss***

Our analysis shows that cities of Malaysia exhibit a daytime β_{HI} of 0.057 °C/decade. Situated in tropical climates, these cities face high risks associated with urban overheating. In this context, β_{HI} has the potential to increase the number of ‘Danger’ days (HI > 41 °C; ref. 20), owing to the high sensitivity of the frequency of high temperatures to changes in the mean value[21,22].

We further examined the β_{HI}-induced increase in ‘Danger’ days in Malaysian cities over the past two decades. Specifically, we first screened *in-situ* SAT and RH observations obtained from the HadISD dataset through rigorous quality control procedures (see Materials and methods), and quantified daily HI during summer daytime for all urban stations. We labeled those days with HI above 41 °C as ‘Danger’[20]. To examine the β_{HI}-induced increase in ‘Danger’ days, we first conducted an overlay analysis by combining the β_{HI}-induced HI amplification and the original yearly HI, and then re-identified the number of ‘Danger’ days with HI exceeding 41 °C. Subsequently, we quantified the difference between these two identified heat day numbers and examined the urban browning-induced increase in ‘Danger’ days in Malaysian cities. Our analysis shows that the days labeled as ‘Danger’ have increased from 1908 to 1964 (i.e., 56 days) in all Malaysian cities from 2003 to 2020.

<u>Note S6</u>: *Insights from China's and India's greening efforts for cooling cities*

Our assessments reveal that over the past two decades, China's and India's cities have undergone significant economic growth (Fig. 4c), yet accompanied by either greening-induced cooling or marginal warming (Fig. 3a,b; Fig. 4c). In China, this is likely driven by a nationwide policy framework that prioritizes the protection of green infrastructure during urbanization, often referred to as ‘ecological civilization construction’. Examples include the National Garden City program initiated in 1992 and its upgrade iterations[23], the 2004 National Forest City program alongside relevant regulations[24], the 2014 Sponge City urban planning program[25], and the 2016 National Ecological Garden City program[26], which incentivize local authorities to protect and cultivate urban green spaces, and has effectively mitigated excessive heat within urban surfaces. Likewise, India has implemented national policies like the 2014 Urban Greening Guidelines[27], accompanied by localized initiatives including city-specific greening programs and ecological restoration projects[28]. While these successful national policies may not be directly translatable to other Global South countries due to differing socio-political and economic contexts, the context-specific, nature-inspired insights and solutions from greening efforts in many Chinese and Indian cities can offer valuable examples for cities with similar economic statuses or constrained resources.

Specifically, urban vegetation typically provides more significant cooling benefits in densely populated areas[29]. However, these areas often face limitations in space for vegetation expansion. To address this, cities with greater economic resources can draw valuable lessons from successful implementations in Beijing and Guangzhou, China, and New Delhi, India. Effective strategies include repurposing abandoned or degraded lands into forest parks or national parks and implementing green roofs to achieve urban cooling. Additionally, bolstering government investment, providing green subsidies, and adopting a balanced approach to integrating native and non-native species also represent effective strategies for urban greening efforts (e.g., Bangalore, India; ref. 30).

Conversely, in cities with more constrained resources, large-scale projects such as converting abandoned mines and degraded sites may be less feasible due to socio-political constraints (e.g., land use rights). In these contexts, focusing on small-scale and dispersed greening strategies may be more practical[31]. Cities like Luoyang and Nanchong in China, and Varanasi in India offer actionable pathways, including planting cost-effective vegetation along roadsides, community borders, and vacant plots, as well as developing micro-greenspaces and pocket parks[32,33,34]. In arid cities with limited water resources, cultivating drought-resilient plants (e.g., Shihezi in China) can be effective, while coastal cities might prioritize wind-resistant and salt-tolerant species to establish protective forest belts (e.g., Fuzhou in China). Economically constrained cities can also benefit from cost-effective initiatives such as public awareness campaigns, urban gardening education, and affordable seedling distribution[35].

Moreover, cities with lower economic resources can adapt successful strategies from wealthier cities to their own socio-political and economic contexts[36]. For instance, the C40 Cities Climate Action Planning Group, which facilitates knowledge exchange among diverse global cities (https://www.c40.org/cities/), demonstrates how resource-constrained cities like Rio de Janeiro and Johannesburg have successfully implemented greening strategies by drawing insights from wealthier cities such as repurposing abandoned sites and fostering community engagement[37,38]. These examples underscore the potential for cross-city knowledge transfer to address varying economic challenges.

However, it is essential to note that here we only qualitatively discussed the potentials for knowledge exchange of urban greening concepts among cities to effectively mitigating urban heat. Policymakers should adapt these nature-inspired concepts and experiences to their specific local contexts to inform sustainable urban cooling solutions.

<u>Note S7</u>: *Limitations of this study*

We acknowledge several limitations in this study. First, our analysis of urban heat stress trends is confined to the past two decades, which may be insufficient to fully capture the long-terms dynamics of urban thermal environments and their interactions with urban greening. This is particularly pertinent for Global South cities due to their ongoing urbanization that began several decades ago[39,40]. Second, while the inclusion of a scaling factor (ε_{UGC}) helps mitigate potential uncertainties arising from adapting a rural-based HI-greenness relationship to urban contexts, this approach may be unable to fully account for urban-rural differences owing to the more complex factors influencing urban greenness (e.g., landscape patterns and phenological changes) relative to their rural counterparts[41,42]. Additionally, urban browning results from a multifaced interplay of various factors. However, the present study has merely quantified the heat stress trends induced by overall observed urban browning, without distinguishing the contributions of each specific factor. Third, substantial agricultural expansion (e.g., oil palm cultivation and coffee farming) in transitional zones of many Global South cities over recent decades have significantly altered regional greenness and impacted local thermal environments[43–46]. While such agricultural activities should have a relatively minimal impact on our primary findings that focus on urban cores, they may introduce uncertainties into our analysis of urban transitional zones due to the lack of differentiation between the impacts from various types of cultivation expansion.

<u>Note S8</u>: *Country typologies identified through four-quadrant plots from physical, physiological, and socioeconomic perspectives*

From a physical perspective, our analysis highlighted two distinct clusters of countries (Fig. 4a; Supplementary Table 1). The first cluster comprises countries indicated by higher browning (K_{EVI}) but relatively lower browning-induced HI amplification (β_{HI}), including Venezuela, Thailand, and Uzbekistan. Conversely, the second category involves countries with lower K_{EVI} yet relatively higher β_{HI}, including Malaysia, Brazil, Argentina, and Chile. From a physiological viewpoint, we pinpointed two distinct categories of countries (Fig. 4b; Supplementary Table 2). The first category encompasses countries with both higher β_{HI} and baseline urban HI values, including Malaysia, Vietnam, and Indonesia. Comparatively, the second category includes countries characterized by higher β_{HI} yet lower baseline urban HI values, including Botswana, Ghana, Côte d'Ivoire, Colombia, Argentina, Brazil, and Mexico. From a socioeconomic standpoint, our analysis also yielded two pivotal categories of countries (Fig. 4c; Supplementary Table 3). The first category includes countries with relatively slower economic growth but larger β_{HI}, including Botswana, Malaysia, Côte d'Ivoire, Colombia, Brazil, and Mexico. In contrast, the second category consists of countries experiencing more rapid economic growth but modest β_{HI}, including China, India, Peru, Turkmenistan, and Uzbekistan.

B. Supplementary Figures

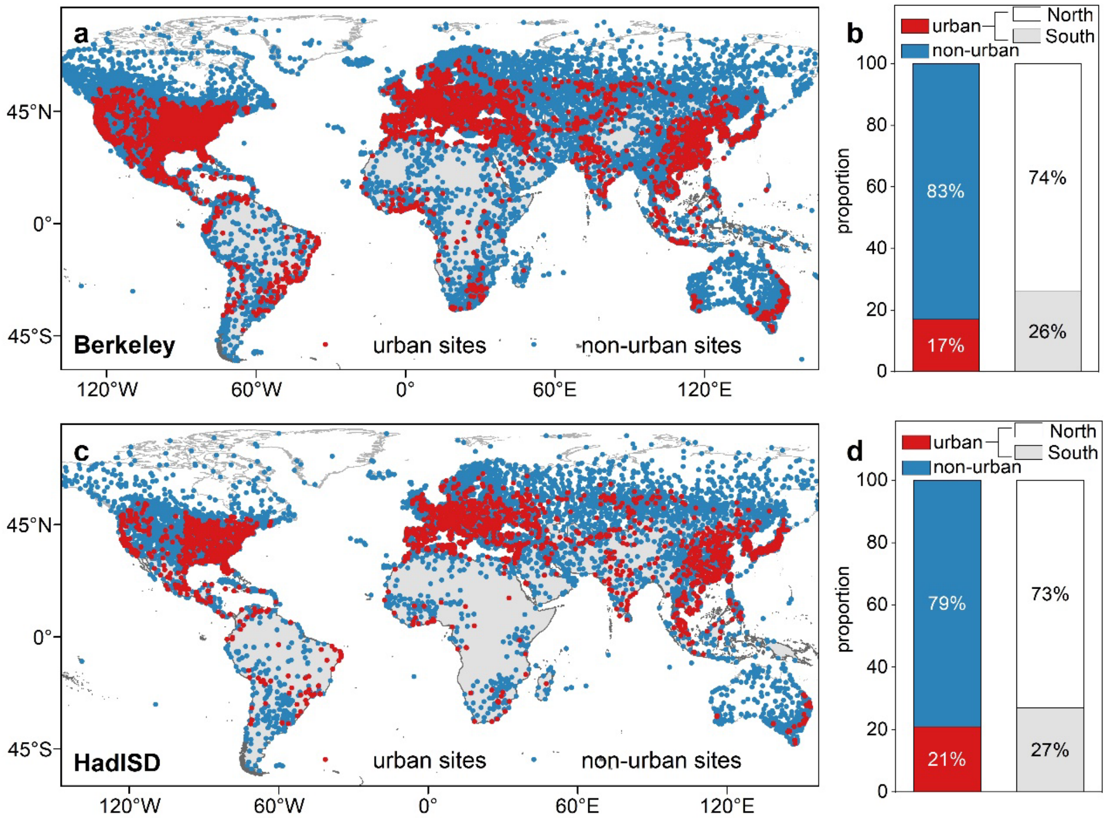

Fig. S1 | Global distribution of meteorological stations. Distributions of urban and rural stations provided by Berkeley Earth dataset (**a**) and HadISD dataset (**c**); proportions of urban and rural stations accounting for all meteorological stations (**b** and **d**); proportions of urban stations within the Global South and Global North (**b** and **d**).

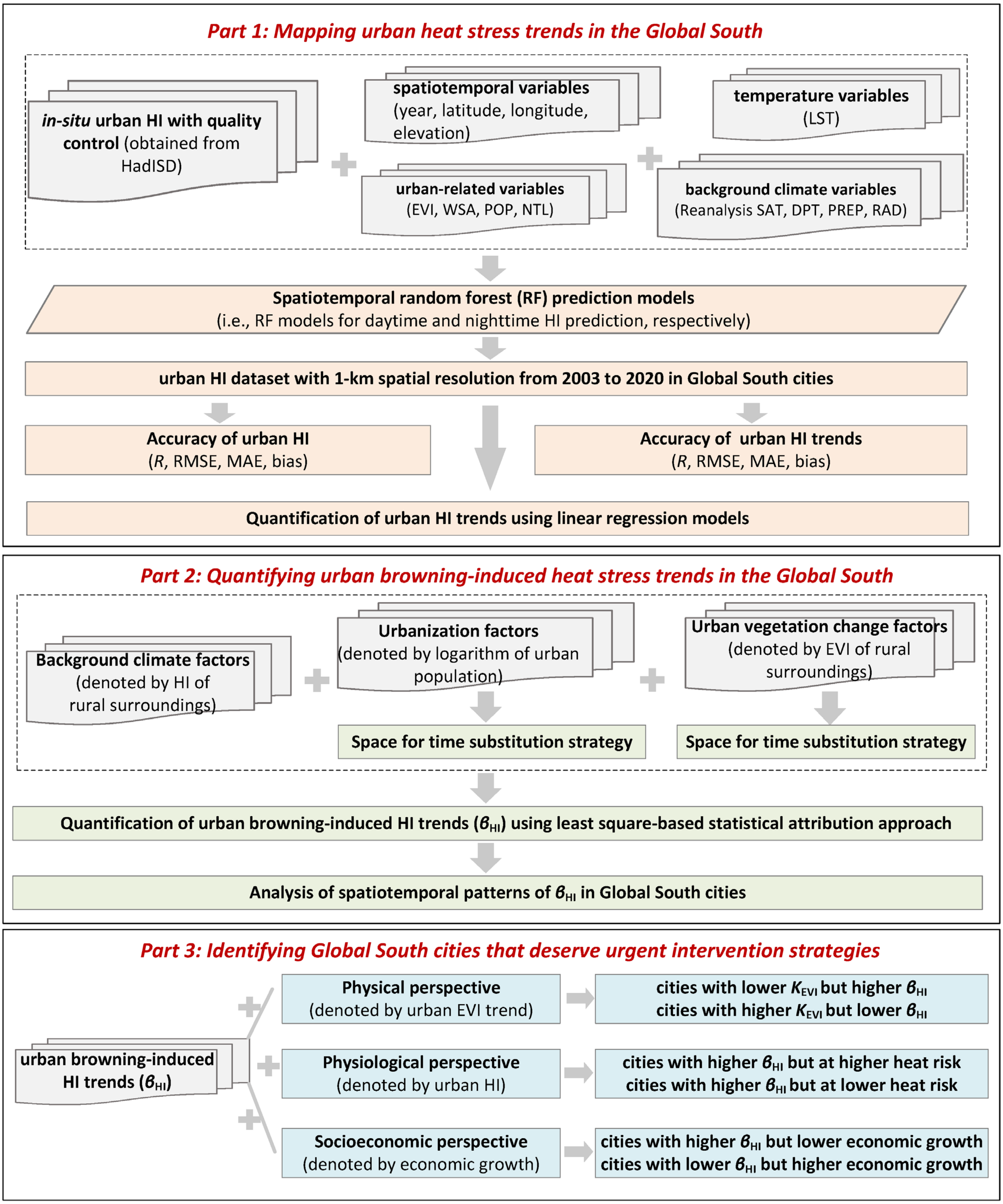

Fig. S2 | Overall framework of our proposed method. This involves three main parts, i.e., mapping urban heat stress trends (K_{HI}) in the Global South (***Part 1***), quantification and analysis of vegetation loss-induced impacts on K_{HI} (***Part 2***), and identification of Global South cities or countries in dire need of intervention to mitigate heat stress induced by urban browning (***Part 3***). ***Part 1*** further includes the generation of 1-km resolution urban HI dataset from 2003 to 2020, validation of the accuracy of urban HI and its long-term trend, as well as the examination of spatiotemporal patterns of K_{HI} across Global South cities.

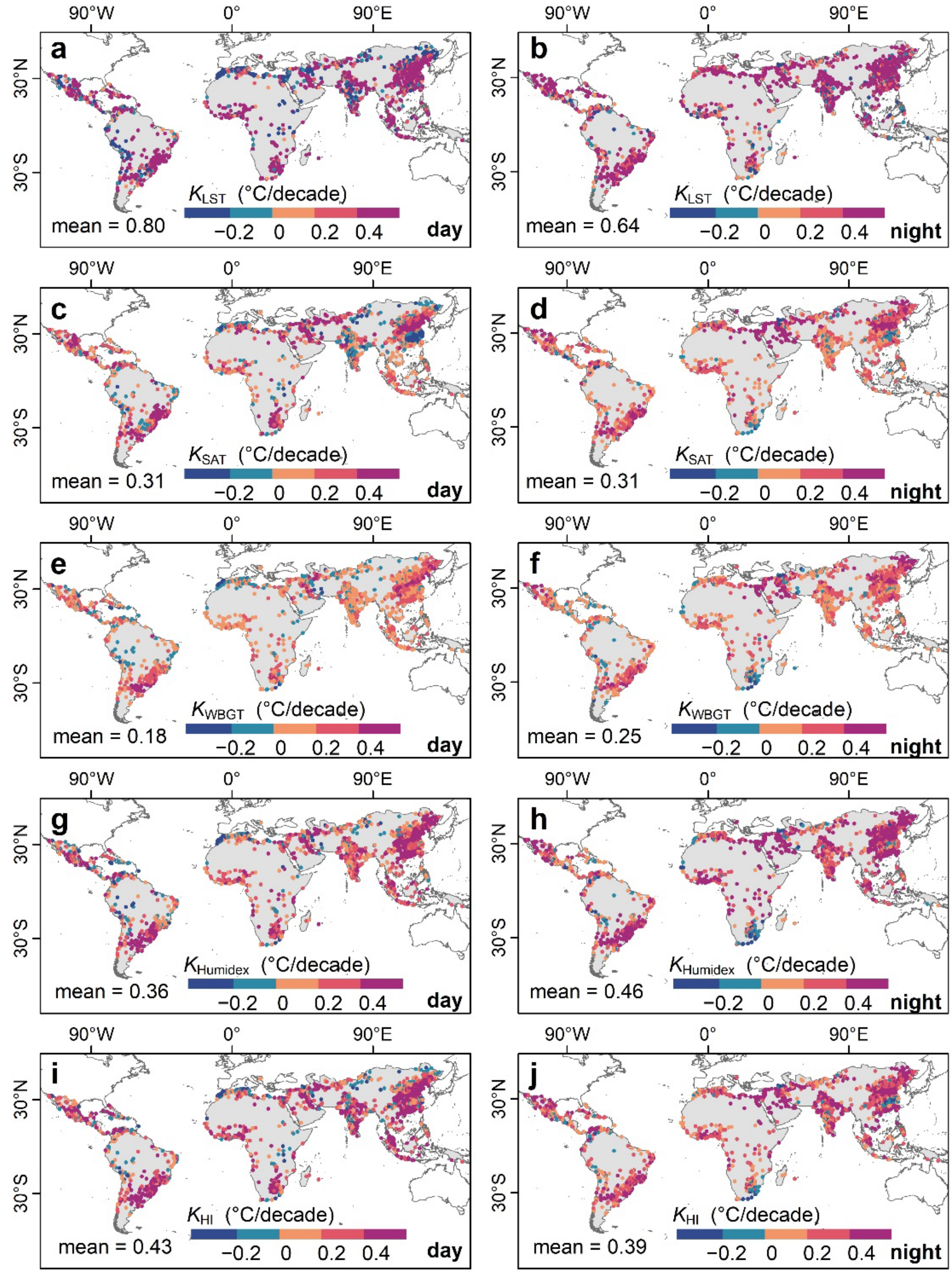

Fig. S3 | Spatiotemporal patterns of urban warming rates quantified based on various temperature metrics across Global South cities. Urban warming trends derived from satellite urban land surface temperature observations (termed K_{LST}; **a** and **b**), urban surface air temperature data (termed K_{SAT}; **c** and **d**), wet-bulb globe temperature in shade conditions at stable wind (termed K_{WBGT}; **e** and **f**), Humidex (termed $K_{Humidex}$; **g** and **h**), and HI (termed K_{HI}; **i** and **j**).

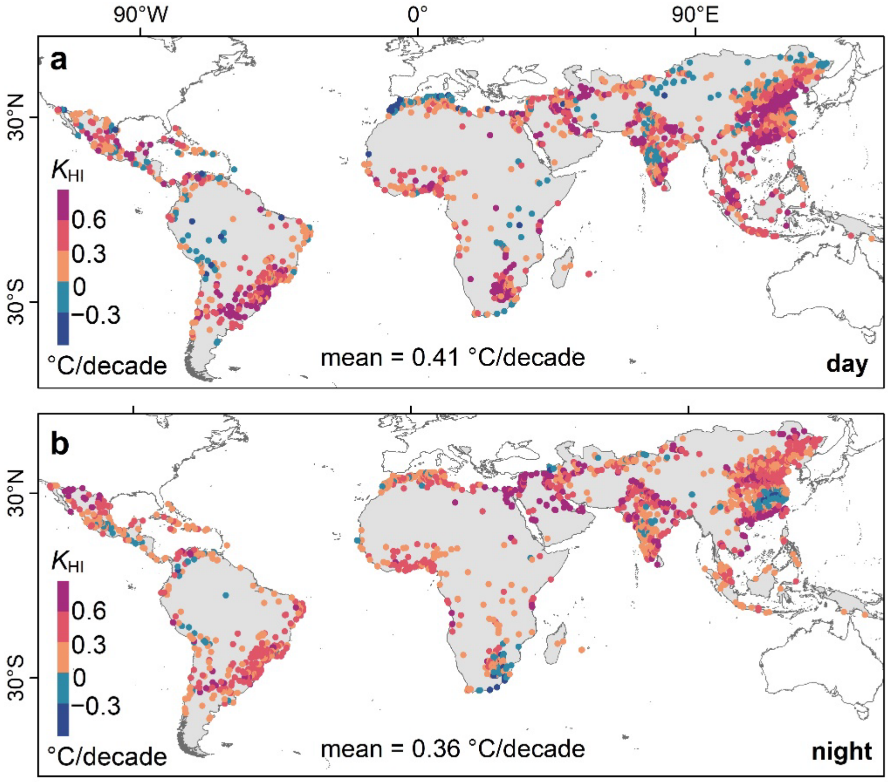

Fig. S4 | Spatiotemporal patterns of K_{HI} for urban transitional zones across the Global South. (**a**) represents the daytime case, and (**b**) represents the nighttime case.

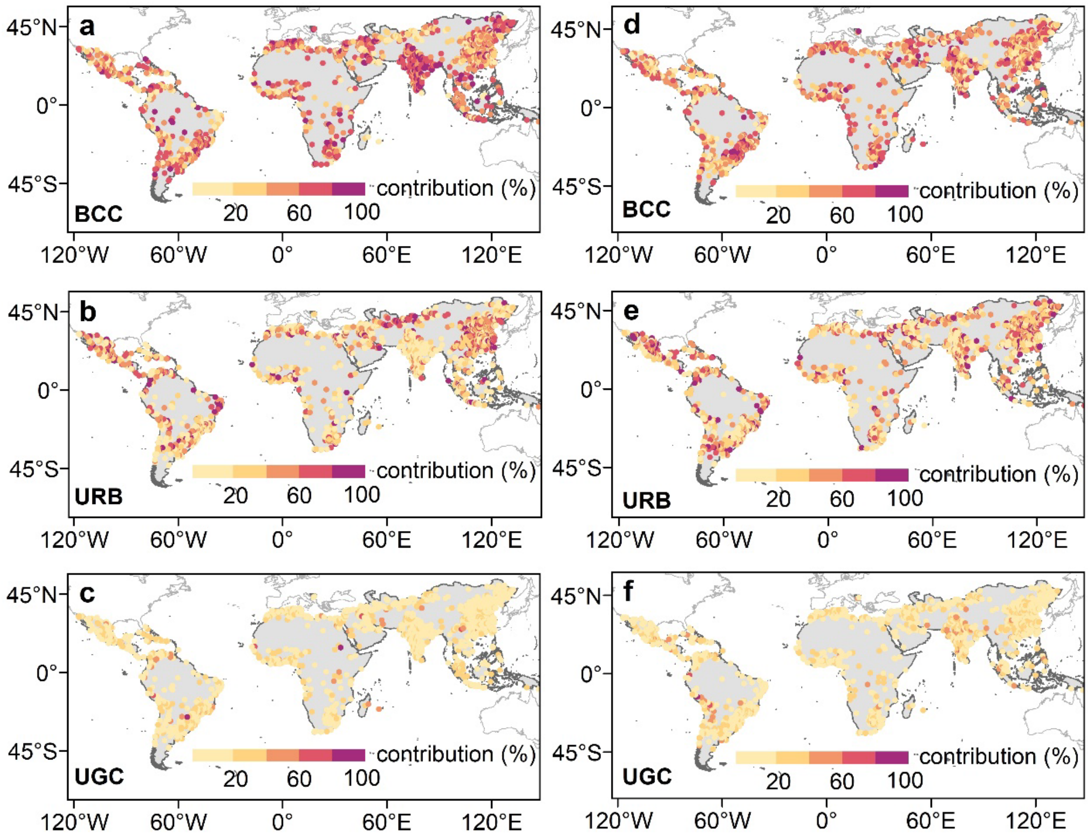

Fig. S5 | Contributions of background climate (BCC), urbanization (URB), and urban greenness change (UGC) factors to K_{HI} across Global South cities. (**a** to **c**) display the daytime case, while (**d** to **f**) display the nighttime case.

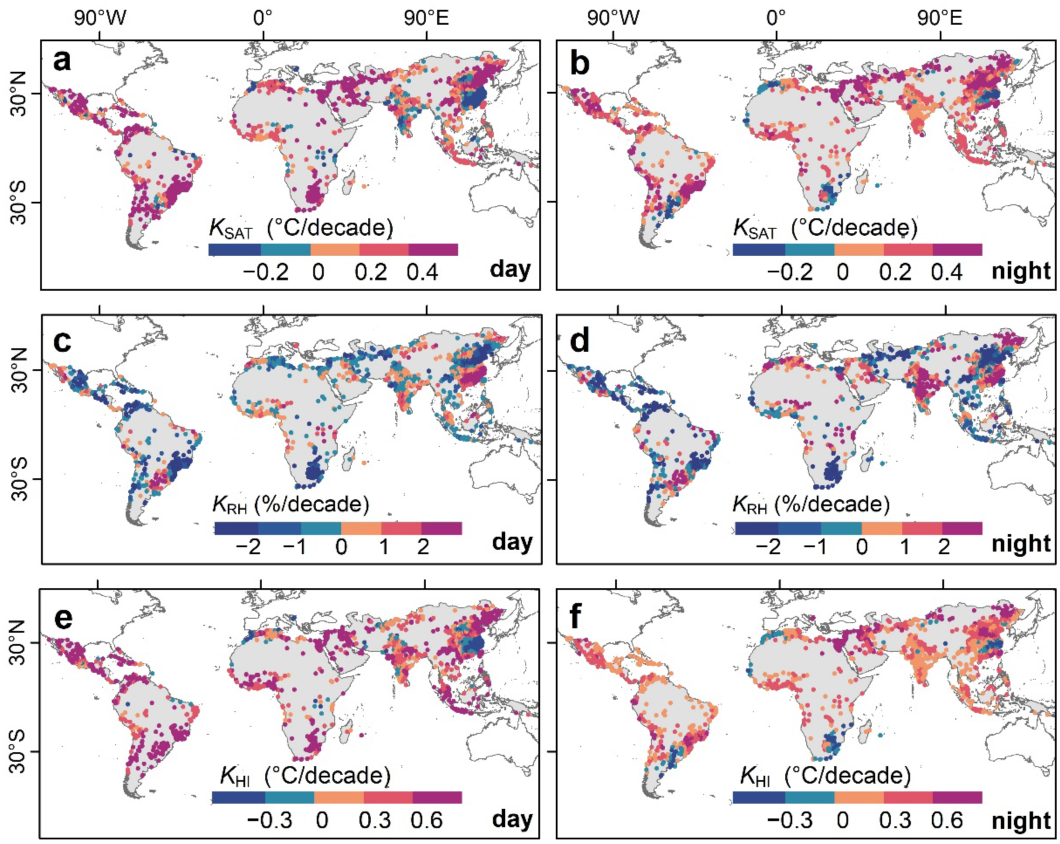

Fig. S6 | Background climate change across the Global South derived from ERA5-Land reanalysis data. Trends in SAT (K_{SAT}; **a** and **b**), RH (K_{RH}; **c** and **d**), and HI (K_{HI}; **e** and **f**) of rural background.

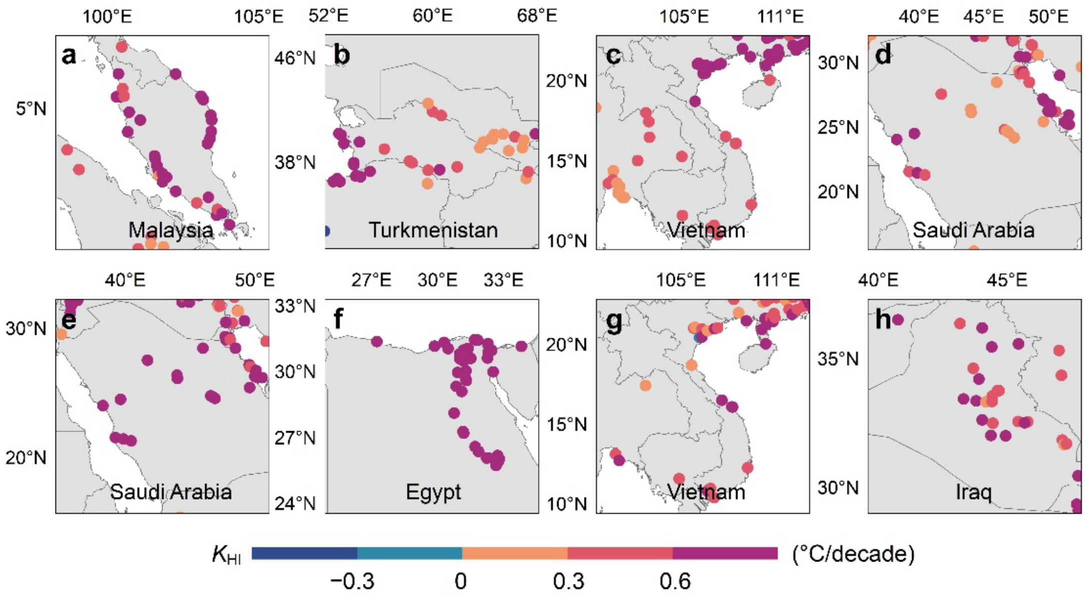

Fig. S7 | Spatiotemporal patterns of K_{HI} across the four countries characterized by the highest mean K_{HI} values. (**a** to **d**) denote the daytime case, while (**e** to **h**) denote the nighttime case.

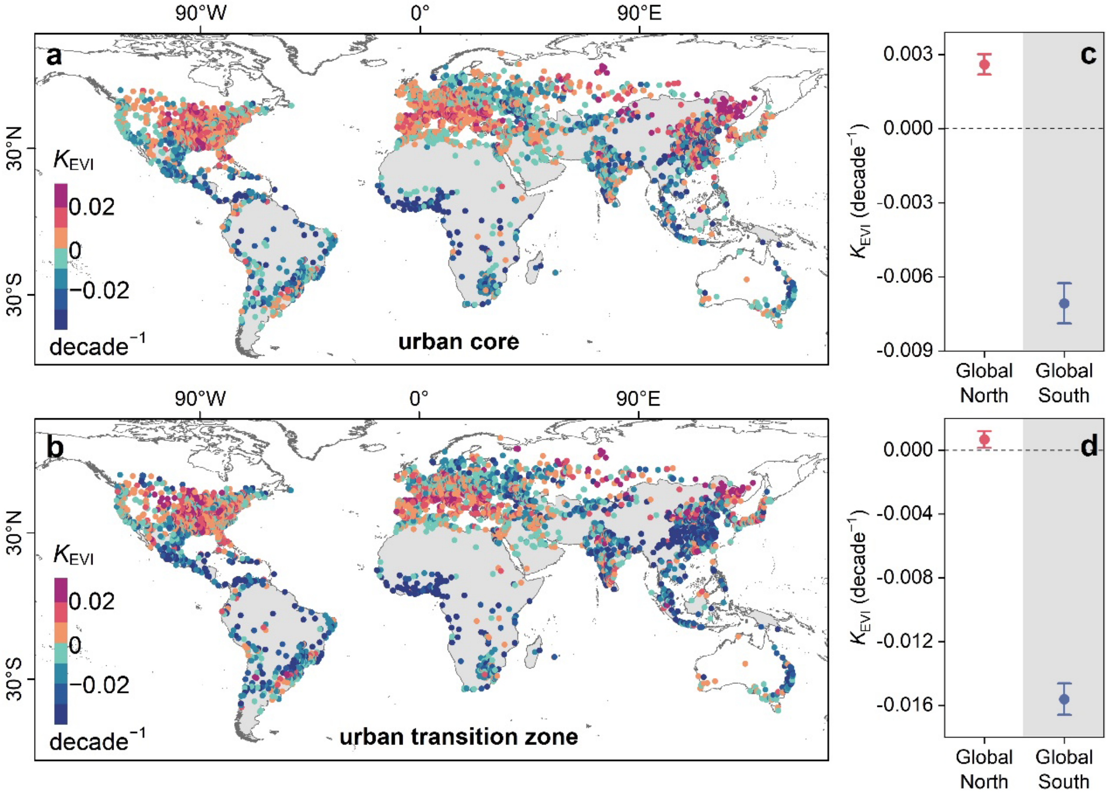

Fig. S8 | Spatiotemporal patterns of the trends in urban greenness (K_{EVI}) across Global South and North cities and their associated mean values. (**a** and **c**) are for urban cores, while (**b** and **d**) are for urban transitional zones. In subplots (**c**) and (**d**), the sample sizes of cities in the Global North and Global South are 3302 and 2341, respectively. The circle denotes the mean value, while the upper and lower bounds of whiskers represent the 95% confidence interval.

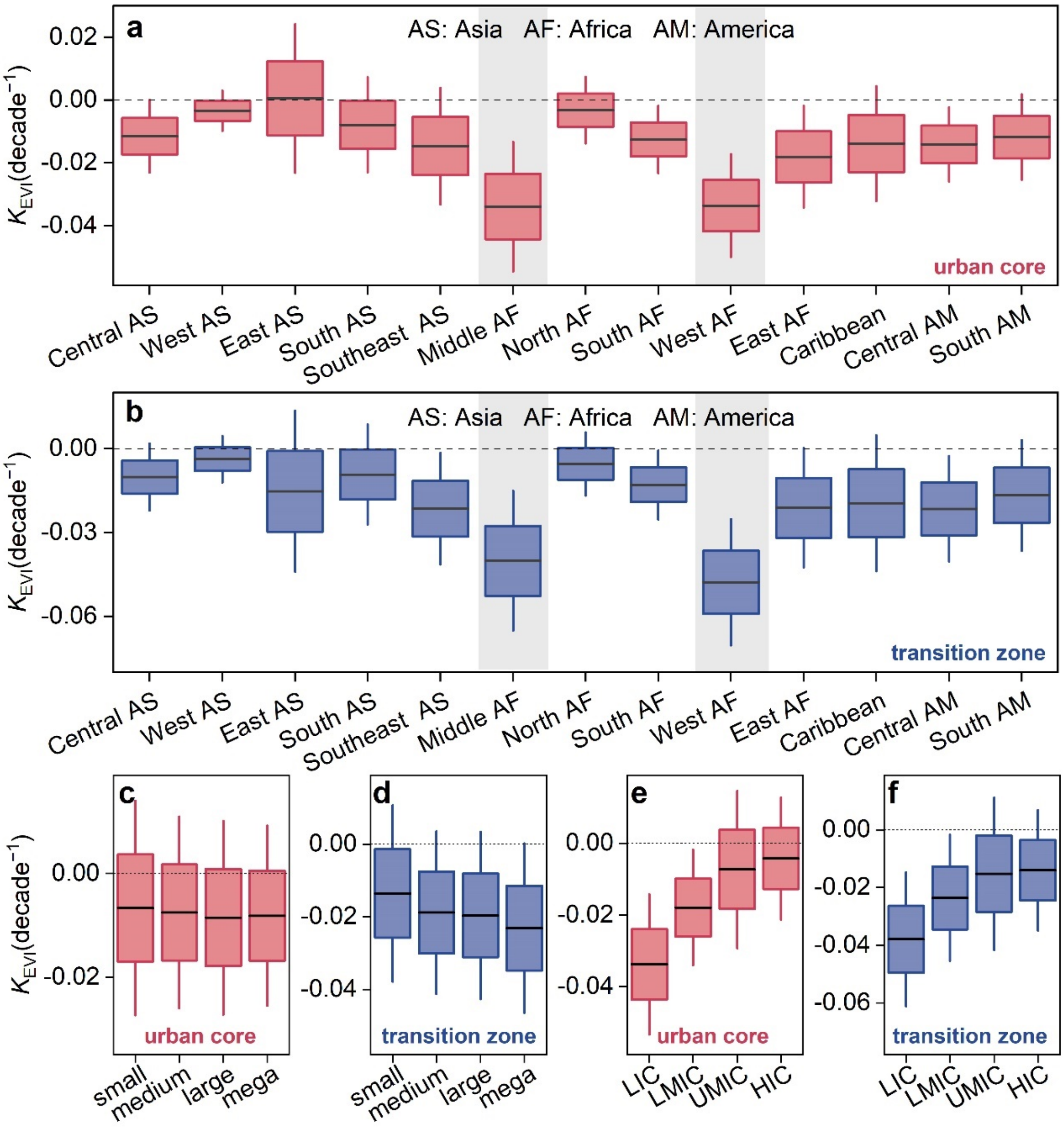

Fig. S9 | Statistics of K_{EVI} across cities within different geographical regions. K_{EVI} in cities within various sub-continents in Global South (**a** for urban core and **b** for urban transition zone). K_{EVI} across cities with different population sizes (termed small, medium, large, and megacities, respectively; **c** for urban core and **d** for urban transition zone); K_{EVI} across cities with diverse economic status, including low income (LIC), low-middle income (LMIC), upper middle income (UMIC), and high income (HIC) cities (**e** for urban core and **f** for urban transition zone). The center line of the box represents the mean, while the lower and upper lines denote 0.5 standard deviations (SD) below and above the mean, respectively. The lower and upper bounds of the whiskers indicate one SD below and above the mean, respectively. In subplots (**a**) and (**b**), the sample sizes of cities in the Central AS, West AS, East AS, South AS, Southeast AS, Middle AF, North AF, South AF, West AF, East AF, Caribbean, Central AM, and South AM are 64, 88, 902, 288, 118, 22, 142, 117, 80, 34, 25, 112, and 336, respectively. In subplots (**c**) and (**d**), the sample sizes of small, medium, large, and mega cities are 1596, 397, 229, and 119, respectively. In subplots (**e**) and (**f**), the sample sizes of LIC, LMIC, UMIC, and HIC cities are 20, 189, 1125, and 1007, respectively.

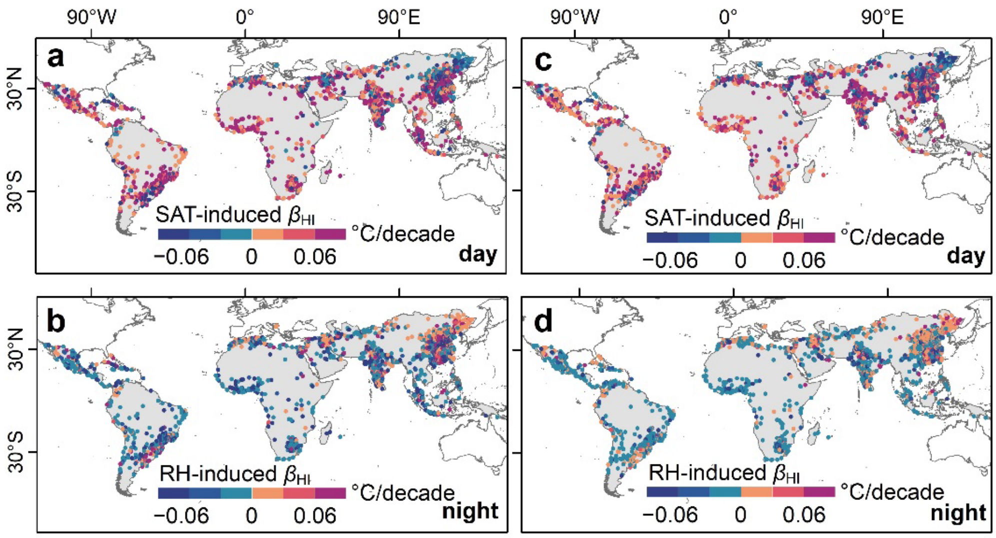

475

476 **Fig. S10 | Browning-induced K_{HI} attributable to the warming effect of surface air**
477 **temperature (SAT) and drying effect of humidity (RH) across Global South**
478 **cities.** (**a**) and (**b**) are for daytime, and (**c**) and (**d**) are for nighttime.

479

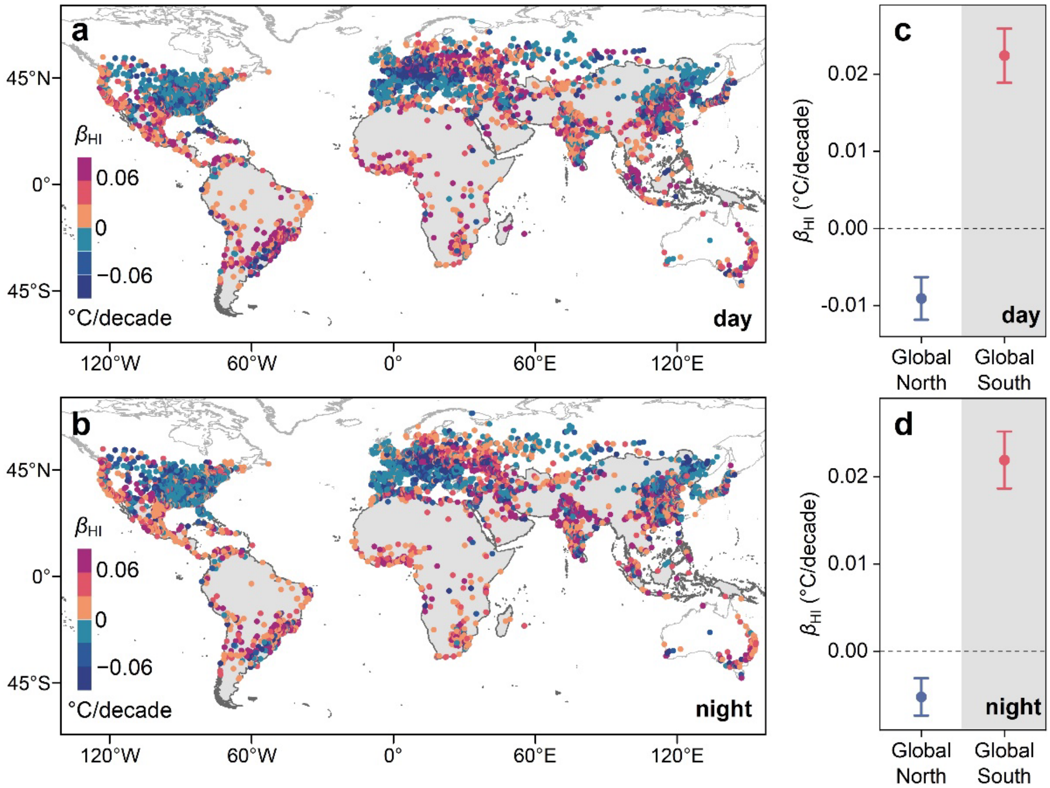

Fig. S11 | Spatiotemporal patterns of urban browning-induced K_{HI} (termed β_{HI}) in cities of Global South and Global North, and their contrasts in mean β_{HI} statistics. (**a** and **c**) are for daytime, and (**b** and **d**) are for nighttime. In subplots (**c**) and (**d**), the circle denotes the mean value, while the upper and lower bounds of whiskers represent the 95% confidence interval. In subplot (**c**), the sample sizes for cities in the Global North and Global South are 3246 and 2321, respectively; while in subplot (**d**), the sample sizes for cities in the Global North and Global South are 3194 and 2261, respectively.

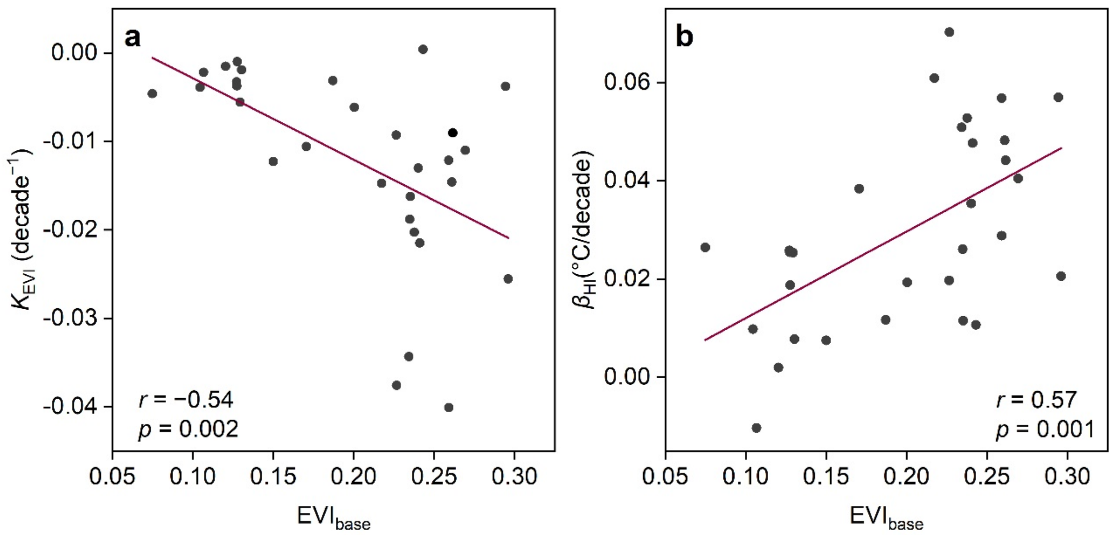

Fig. S12 | Relationships between baseline EVI (EVI_{base}) and urban greenness trend (K_{EVI}; a), as well as between EVI_{base} and browning-induced urban HI trends (β_{HI}; b) during summer daytime across Global South countries. The *r* and *p* values are obtained from a two-sided *t*-test with no adjustments.

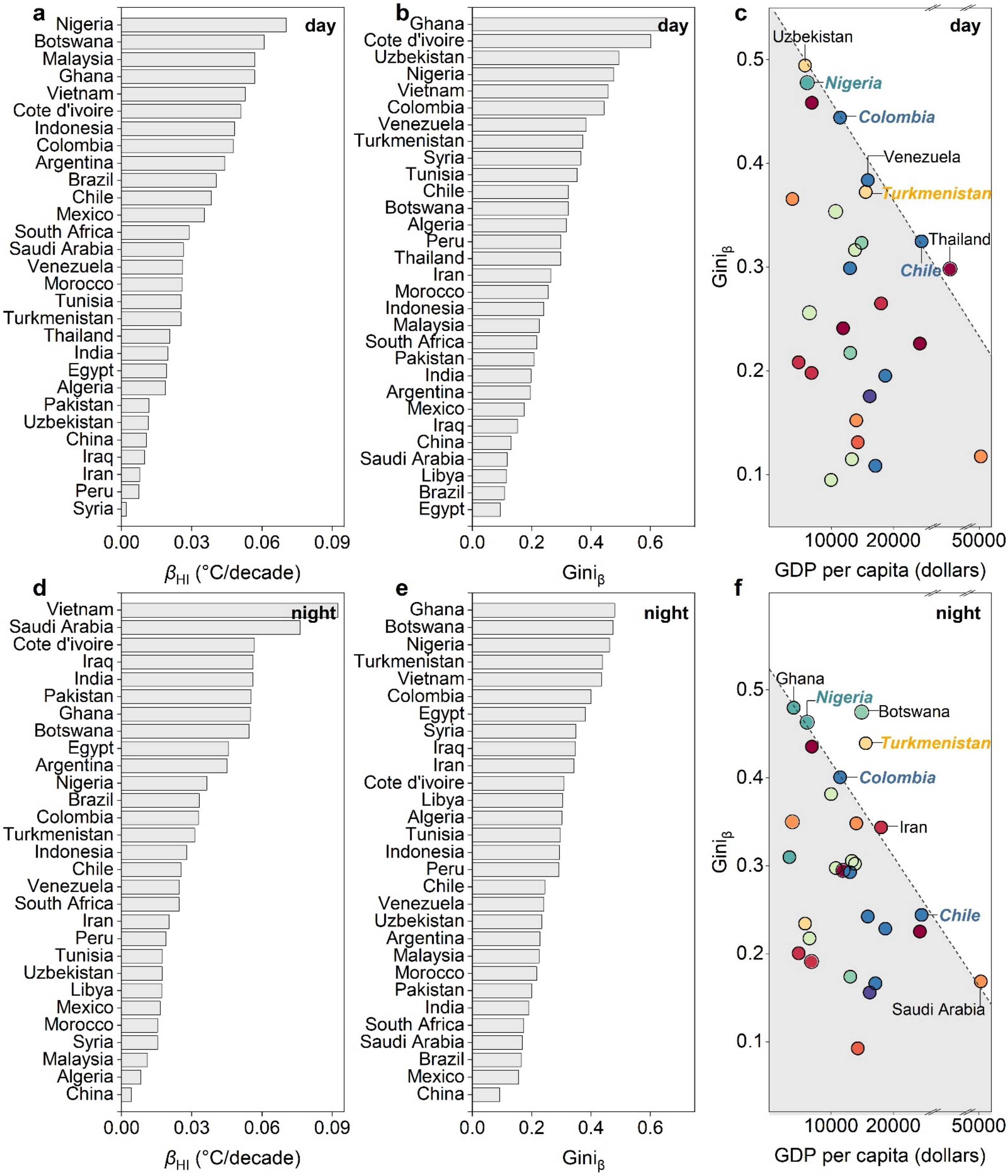

Fig. S13 | Country-level statistics of β_{HI} in Global South cities and associated national inequalities quantified using the Gini index ($Gini_\beta$). β_{HI} and corresponding $Gini_\beta$ for each country during daytime (**a** and **b**) and nighttime (**d** and **e**); Scatterplots illustrating the relationship between $Gini_\beta$ and GDP per capita for all countries during daytime (**c**) and nighttime (**f**). Only the countries with ten or more selected cities were included in this analysis to ensure statistical significance of the estimated β_{HI} values.

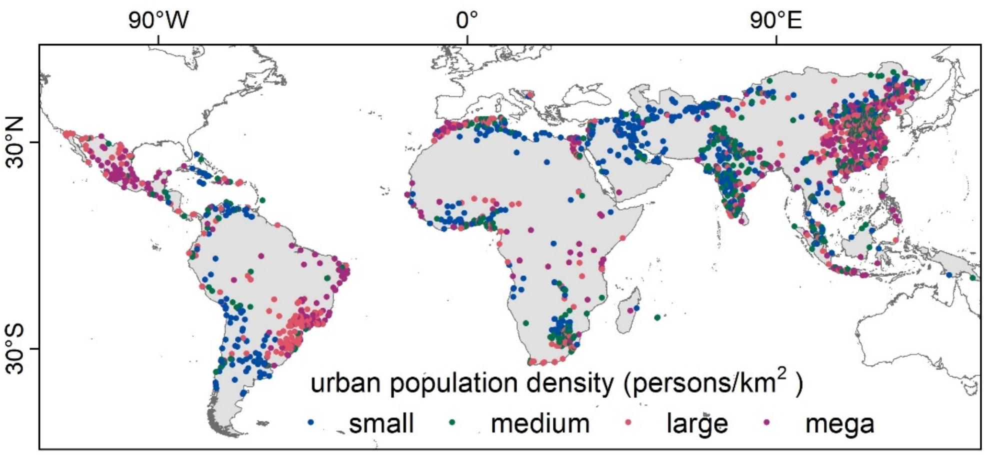

Fig. S14 | Categorization of city sizes based on quartiles of urban population density, termed small cities (< 630 persons/km²), medium cities (630–1,977 persons/km²), large cities (1,977–4,430 persons/km²), and megacities (> 4,430 persons/km²), respectively.

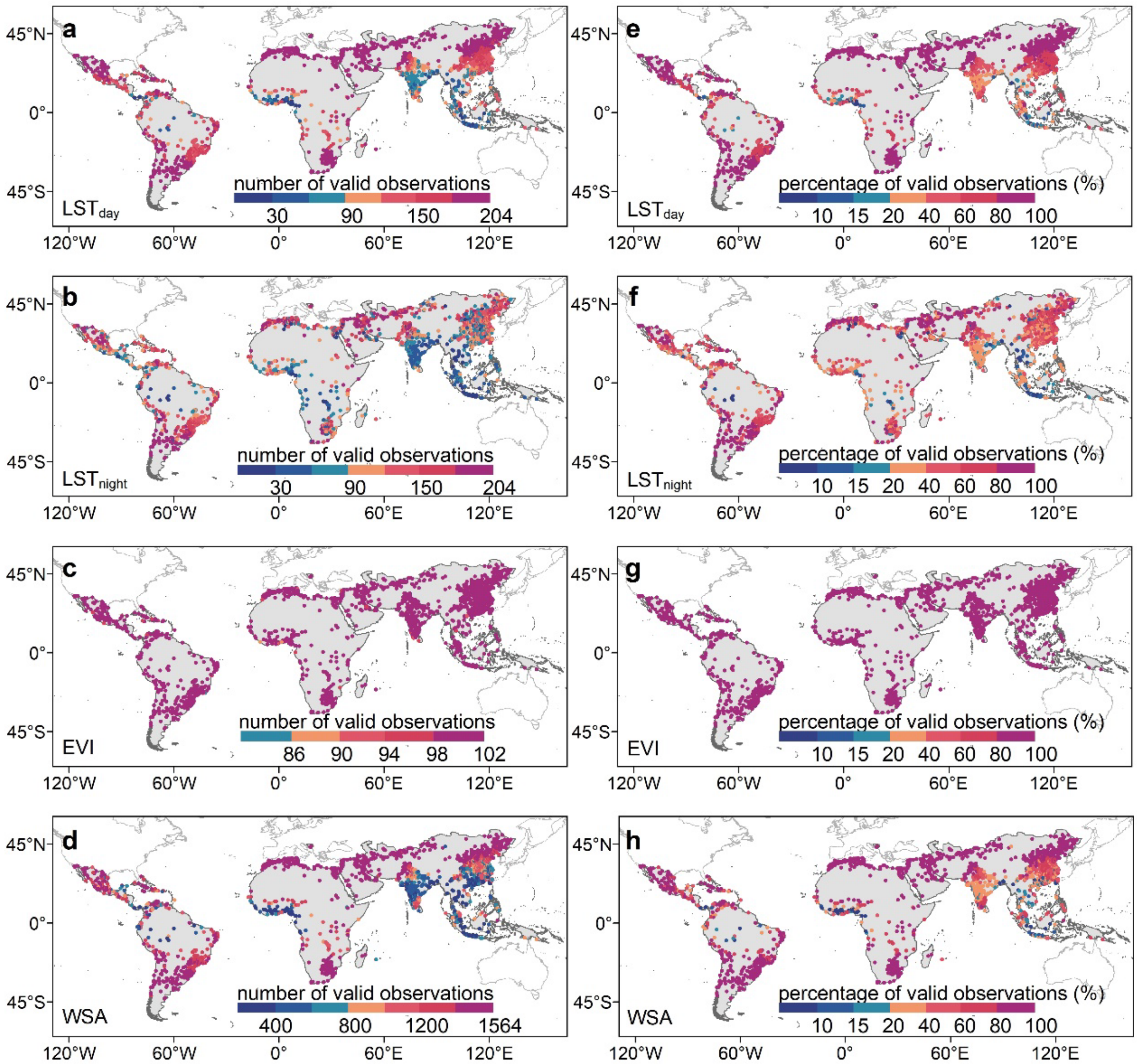

Fig. S15 | Number of valid observation days of LST, EVI, and WSA, and their associated proportions (i.e., the ratio of actual observation days to the maximum possible observation days assuming no missing data) across Global South cities. To eliminate possible impacts arising from cloud contamination or other factors, we only extracted LST observations with a retrieval error of 3.0 K or less based on quality-control bitmask layer, and further utilized these LST observations to mask WSA and EVI observations.

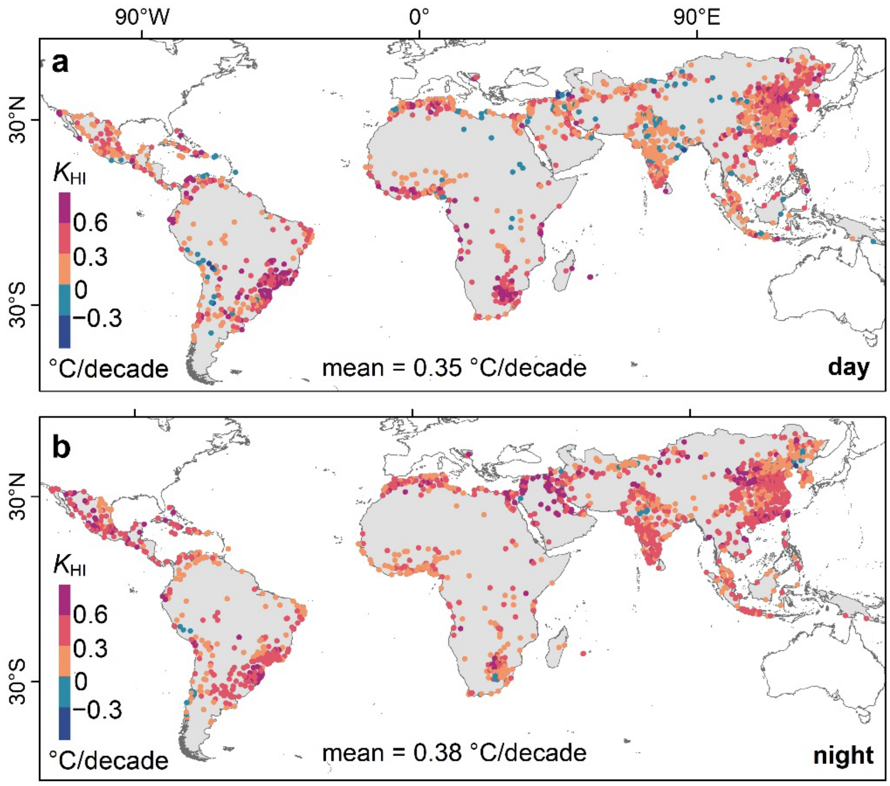

Fig. S16 | Spatiotemporal patterns of annual mean K_{HI} in urban Global South.

(**a**) is for daytime and (**b**) is for nighttime.

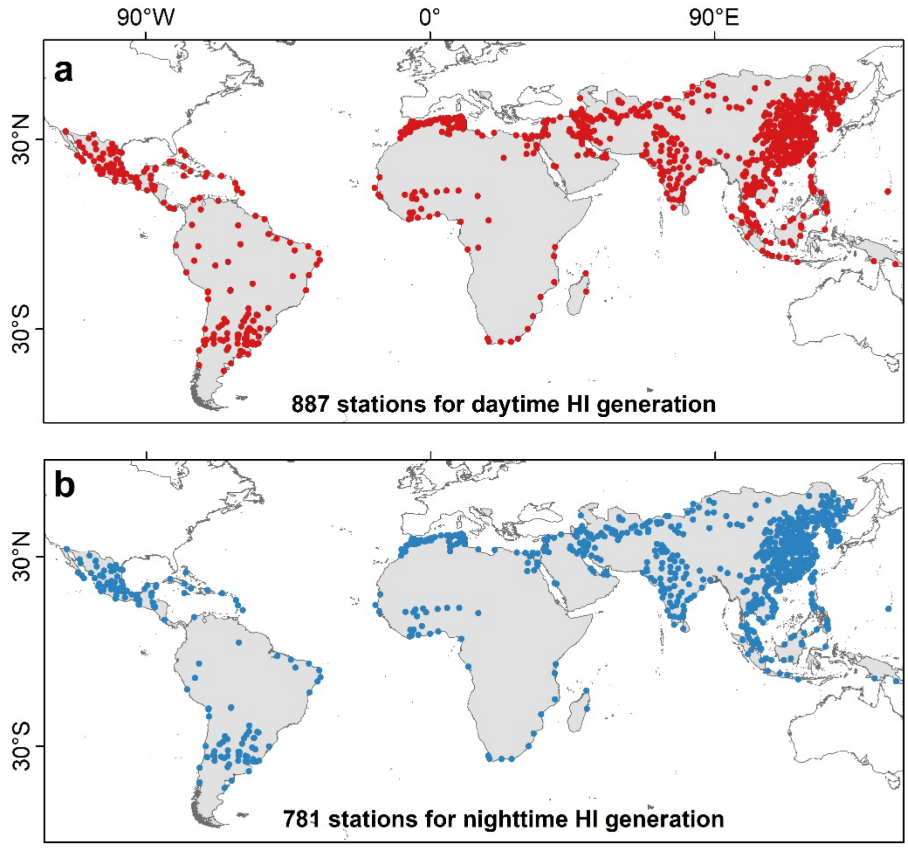

Fig. S17 | Distribution of urban stations employed for generating 1-km resolution urban HI for Global South cities. (**a**) is for daytime and (**b**) is for nighttime.

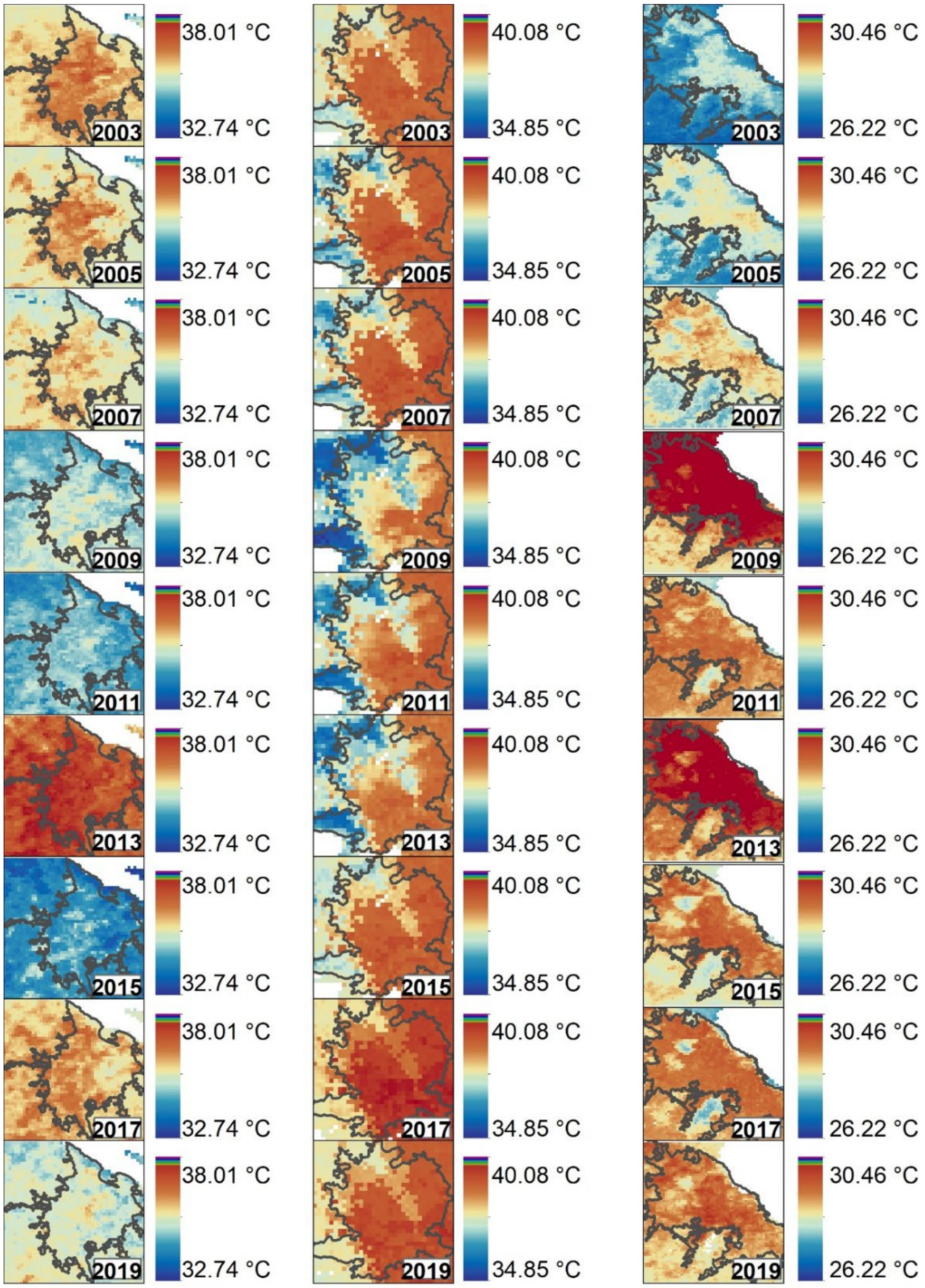

Fig. S18 | Urban HI maps with 1-km spatial resolution for summer daytime in typical cities of the Global South. The three columns showcase Shanghai in China, Riyadh in Saudi Arabia, and Buenos Aires in Argentina, respectively.

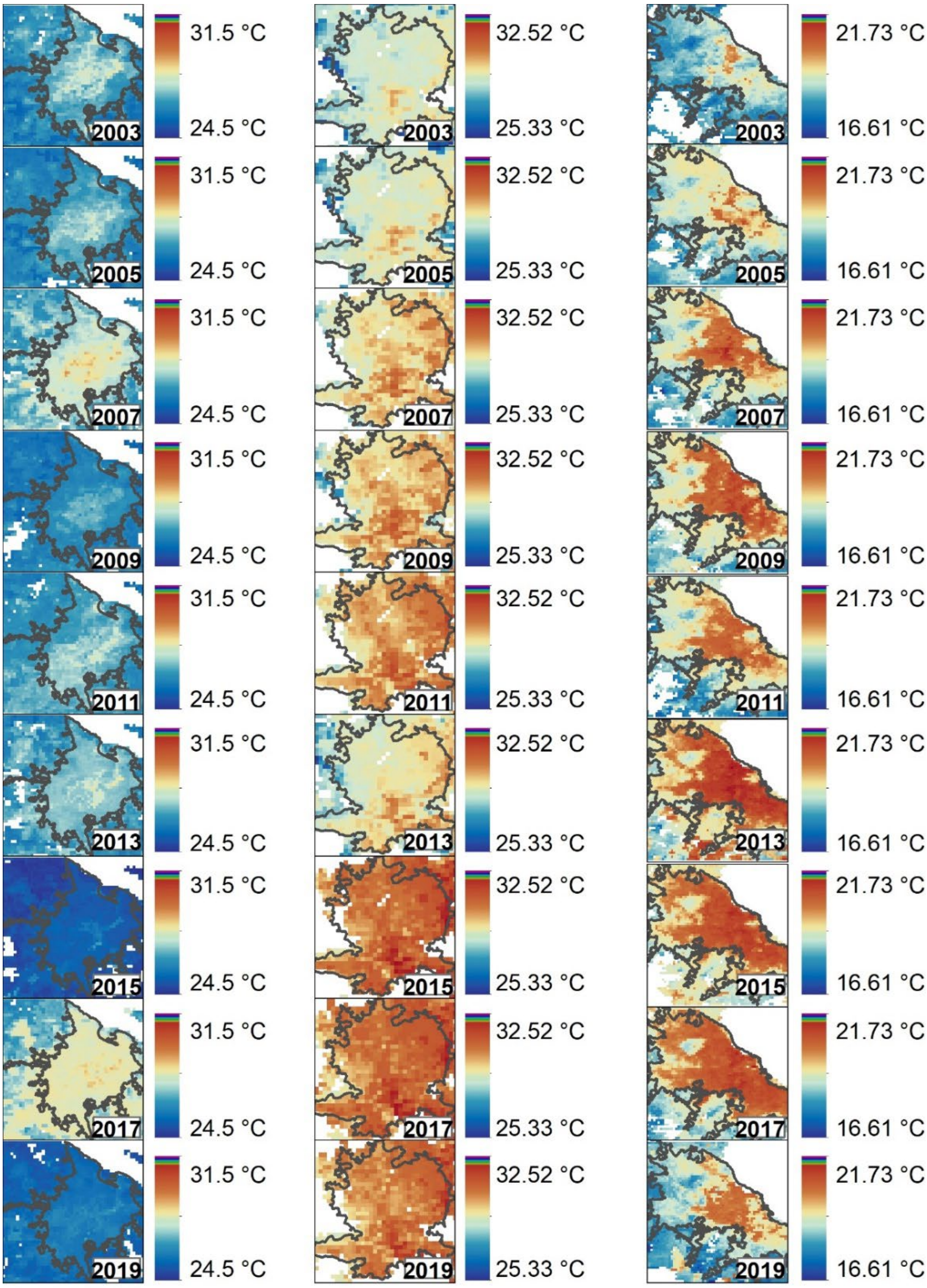

Fig. S19 | Similar to Fig. S18, but for the nighttime case.

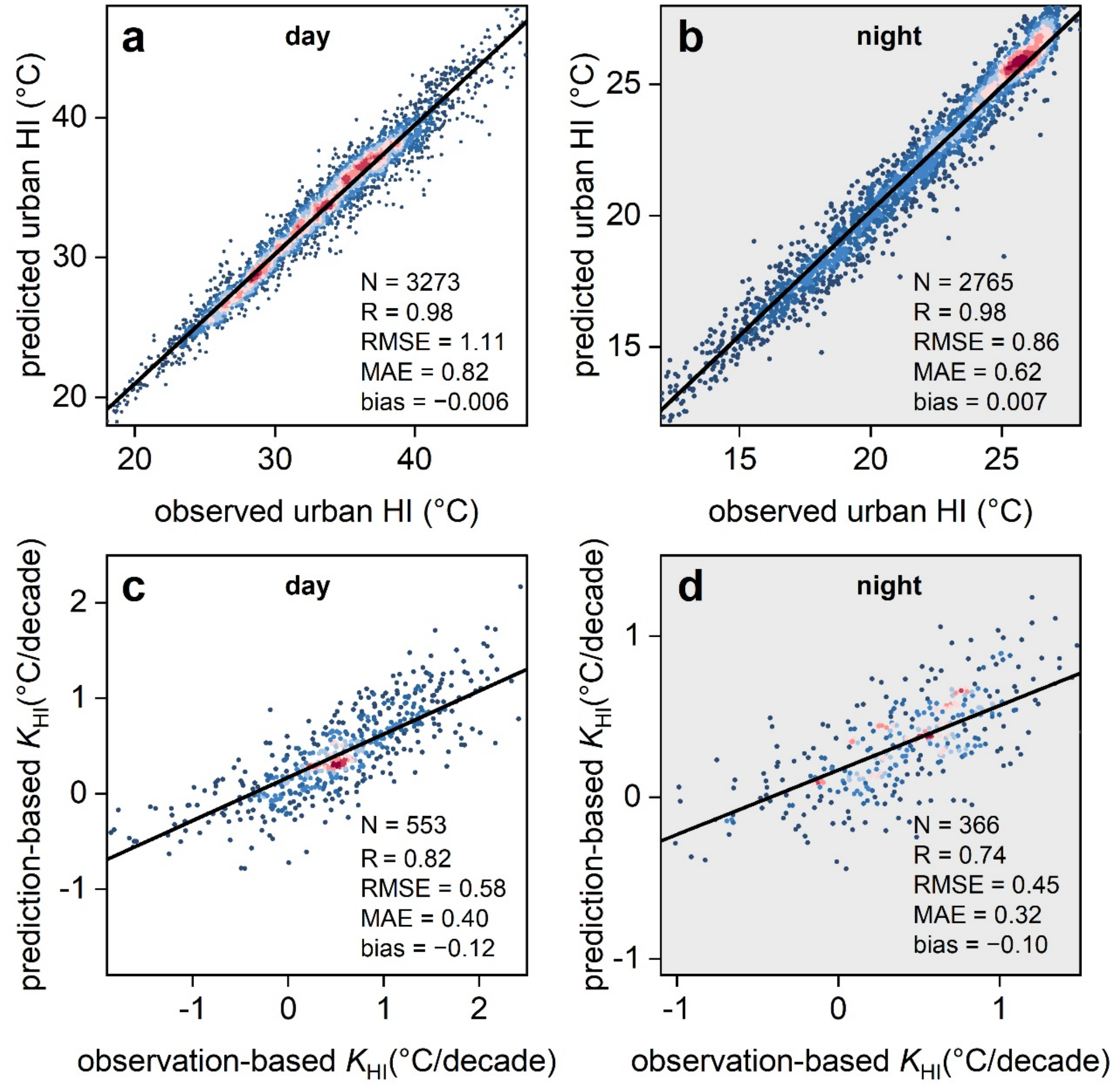

Fig. S20 | Accuracy assessments of urban HI and its associated trends (K_{HI}) across Global South cities. Scatterplots of the observed and predicted urban HI for summer daytime (**a**) and nighttime (**b**); scatterplots of K_{HI} calculated based on the observed and predicted urban HI values for summer daytime (**c**) and nighttime (**d**). N denotes the number of samples used for cross-validation. *R*, RMSE, and MAE signify the correlation coefficient, root mean square error, and mean absolute error between the observed and predicted values, respectively.

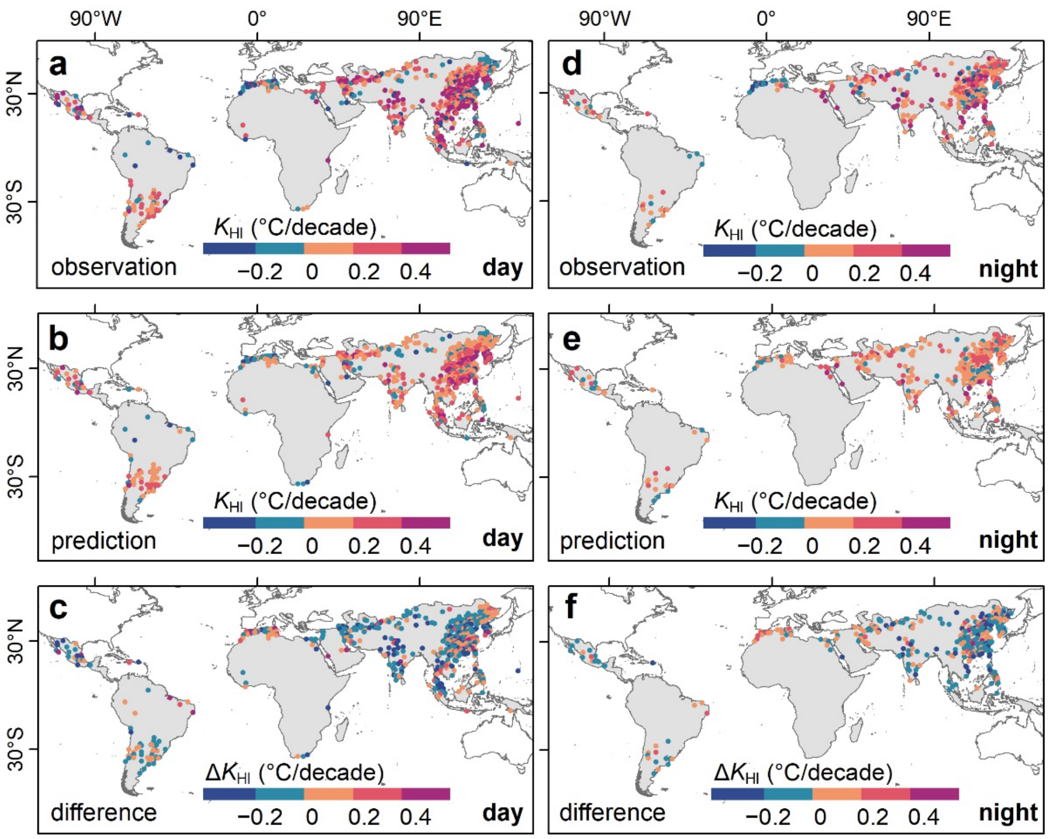

Fig. S21 | Accuracy assessment of K_{HI} across the Global South cities.

Spatiotemporal patterns of K_{HI} estimated from observed (**a** and **d**) and predicted urban HI values (**b** and **e**), as well as their in-between differences (**c** and **f**).

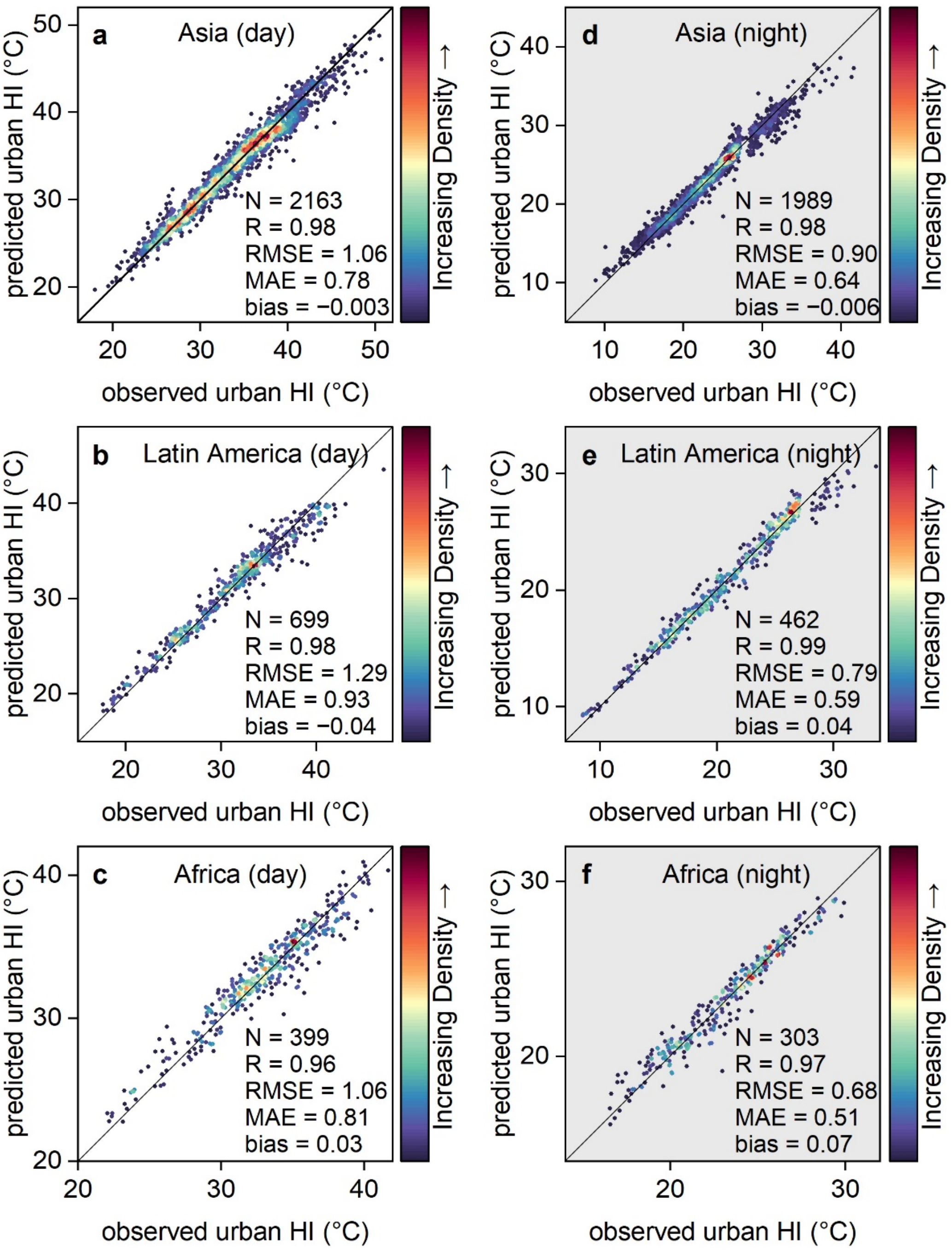

Fig. S22 | Accuracy assessments of urban HI across cities in each sub-continent. Scatterplots of the observed and predicted urban HI for summer daytime and nighttime across Asian cities (**a** and **d**), Latin American cities (**b** and **e**), and African cities (**c** and **f**). *N* denotes the number of samples used for cross-validation. *R*, RMSE, and MAE represent the correlation coefficient, root mean square error, and mean absolute error between observed and predicted values, respectively.

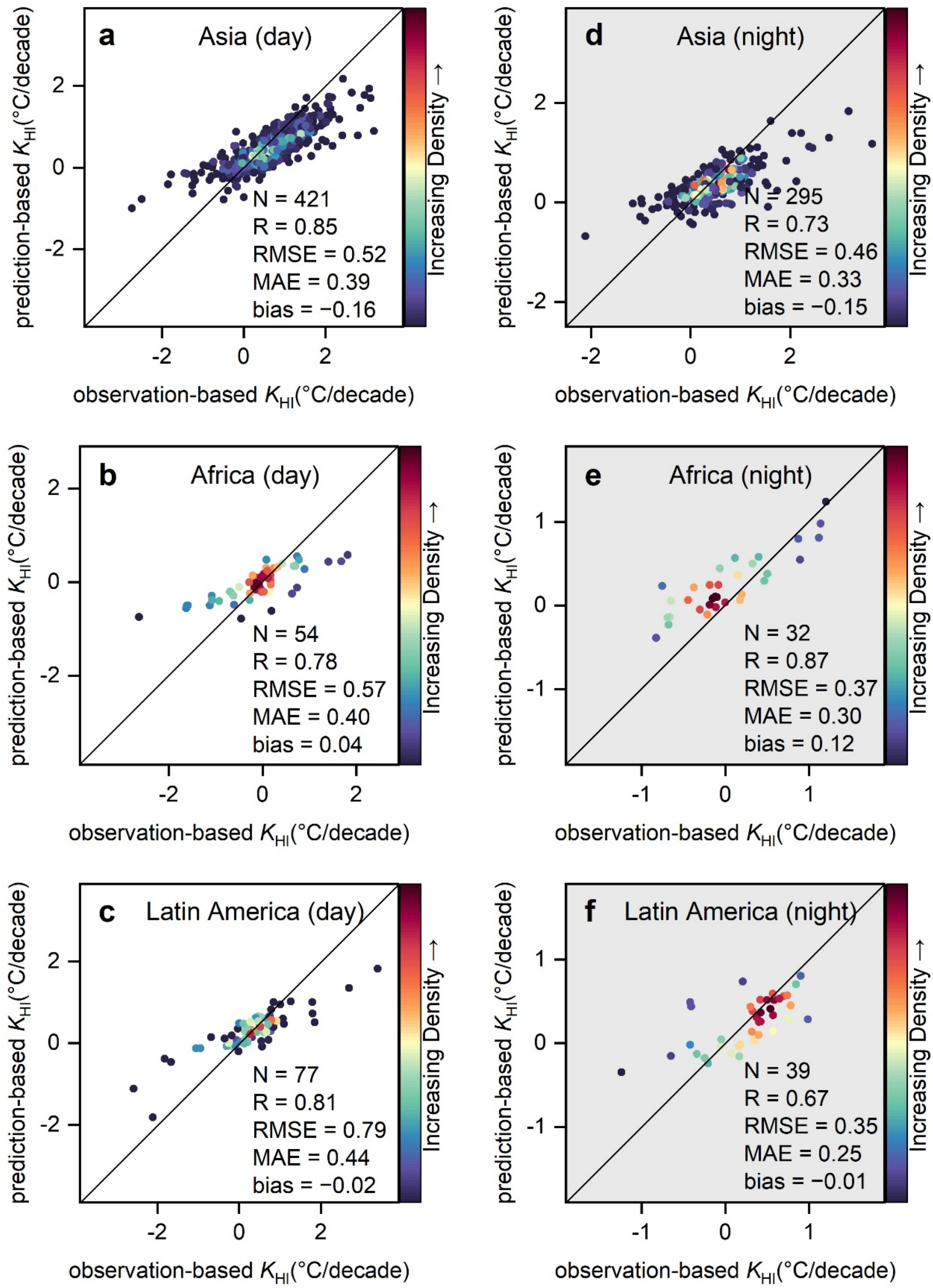

Fig. S23 | Accuracy assessments of urban HI trends (K_{HI}) across cities in each sub-continent. Scatterplots of the observed and predicted K_{HI} for summer daytime and nighttime across Asian cities (**a** and **d**), African cities (**b** and **e**), and Latin American cities (**c** and **f**). *N* denotes the number of samples used for cross-validation.

R, RMSE, and MAE represent the correlation coefficient, root mean square error, and mean absolute error between observed and predicted values, respectively.

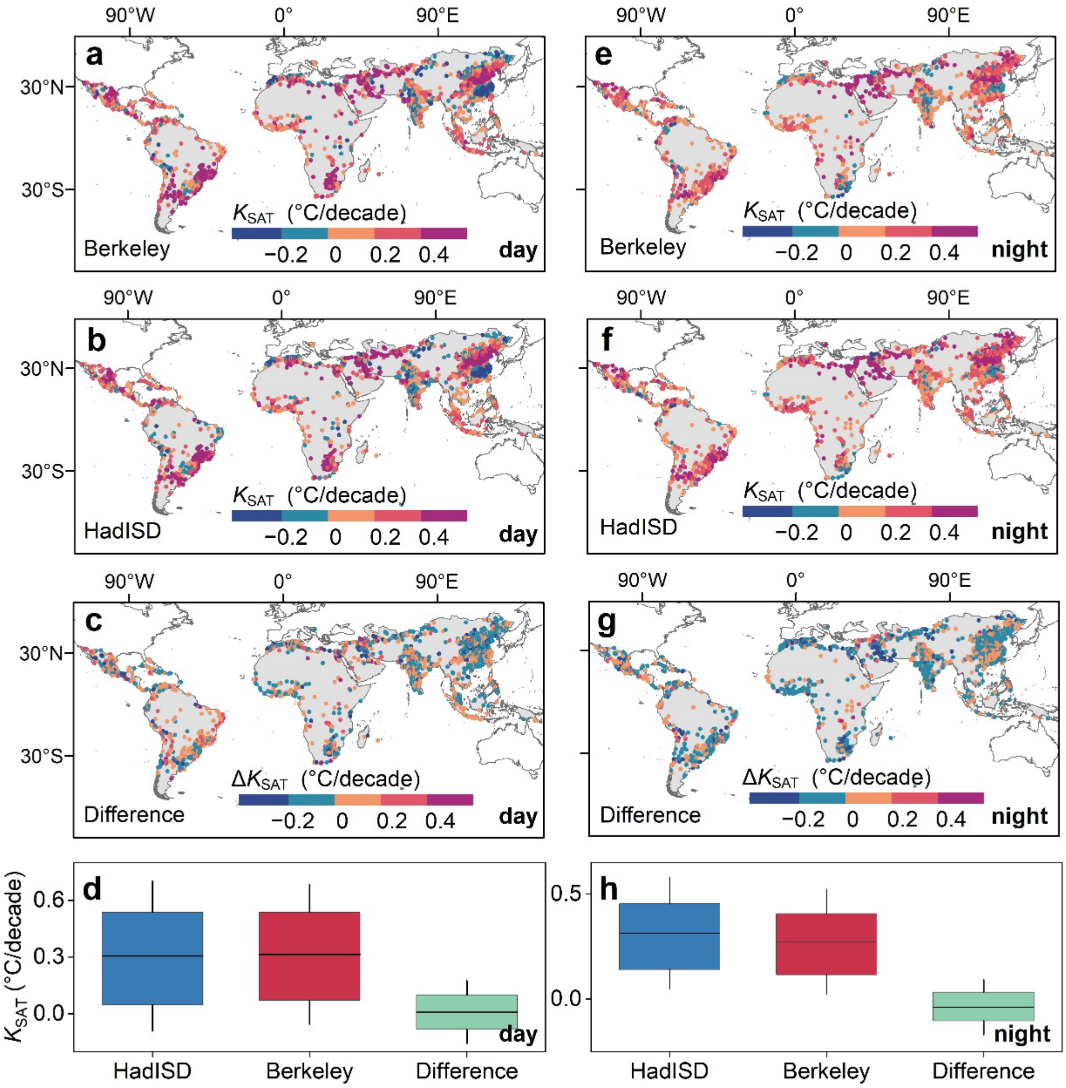

Fig. S24 | Possible uncertainties arising from the relatively limited and sparsely distributed urban stations. Spatiotemporal patterns of K_{SAT} quantified based on *in-situ* observations sourced from Berkeley Earth dataset (**a** and **e**) and HadISD dataset (**c** and **d**), as well as their in-between differences (**b** and **f**); Statistical mean values of K_{SAT} quantified based on these two data sources (**c** and **g**). In subplots (**d**) and (**h**), the center line represents the mean, while the lower and upper lines denote 25th and 75th quantiles, respectively. The lower and upper bounds of the whiskers indicate one standard deviation (SD) below and above the mean, respectively. The city sample size for all boxes in subplot (**d**) is 2322, whereas the sample size for subplot (**h**) is 2,266.

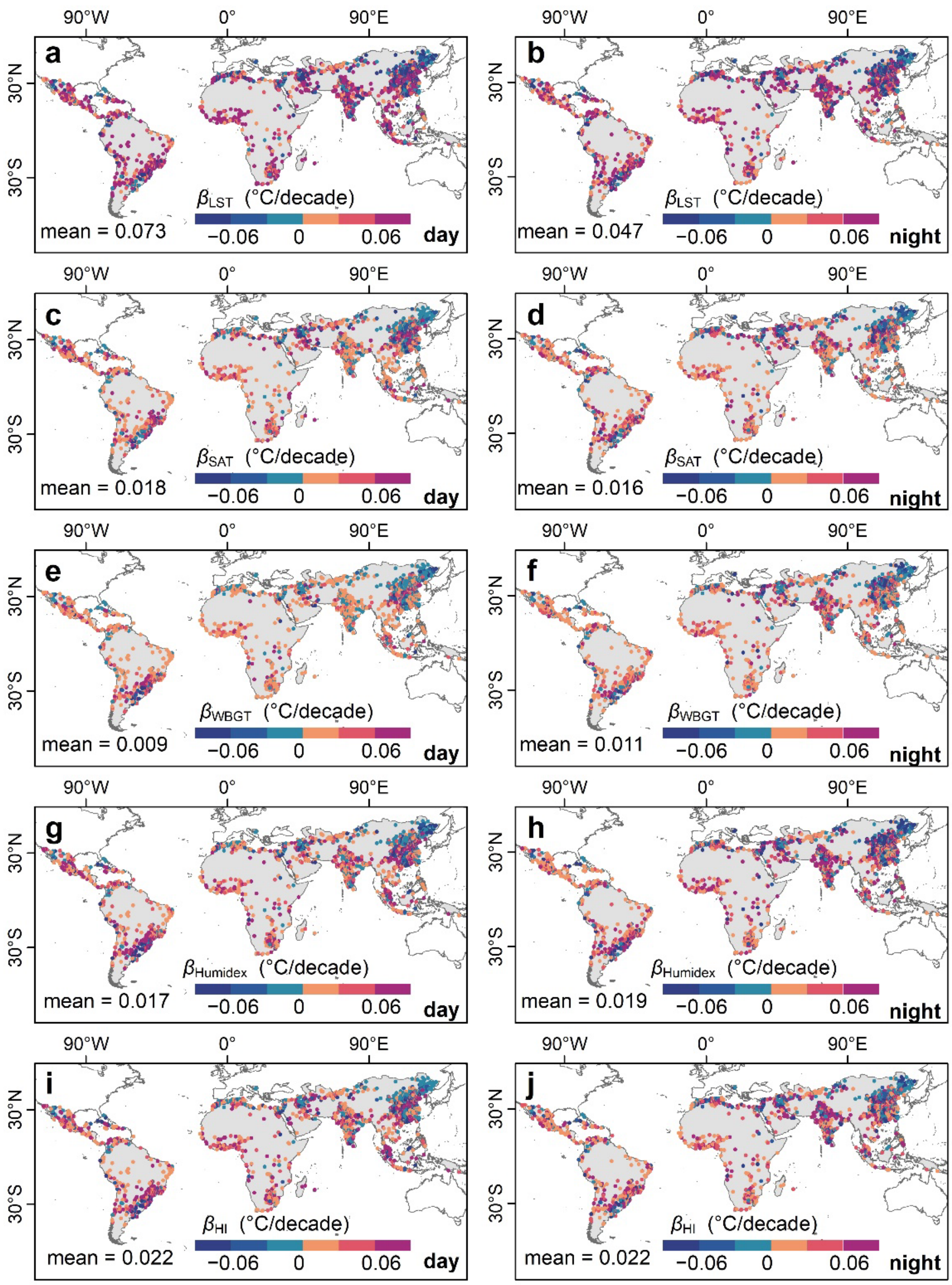

Fig. S25 | Spatiotemporal patterns of urban browning-induced heat stress trends quantified using various temperature or heat indices across Global South cities. Urban browning-induced heat trends derived from satellite urban land surface temperature observations (termed β_{LST}; **a** and **b**), derived from urban surface air temperature data (termed β_{SAT}; **c** and **d**), derived from wet-bulb globe temperature in shade conditions at stable wind (termed β_{WBGT}; **e** and **f**), derived from Humidex (termed β_{Humidex}; **g** and **h**), derived from HI (termed β_{HI}; **i** and **j**).

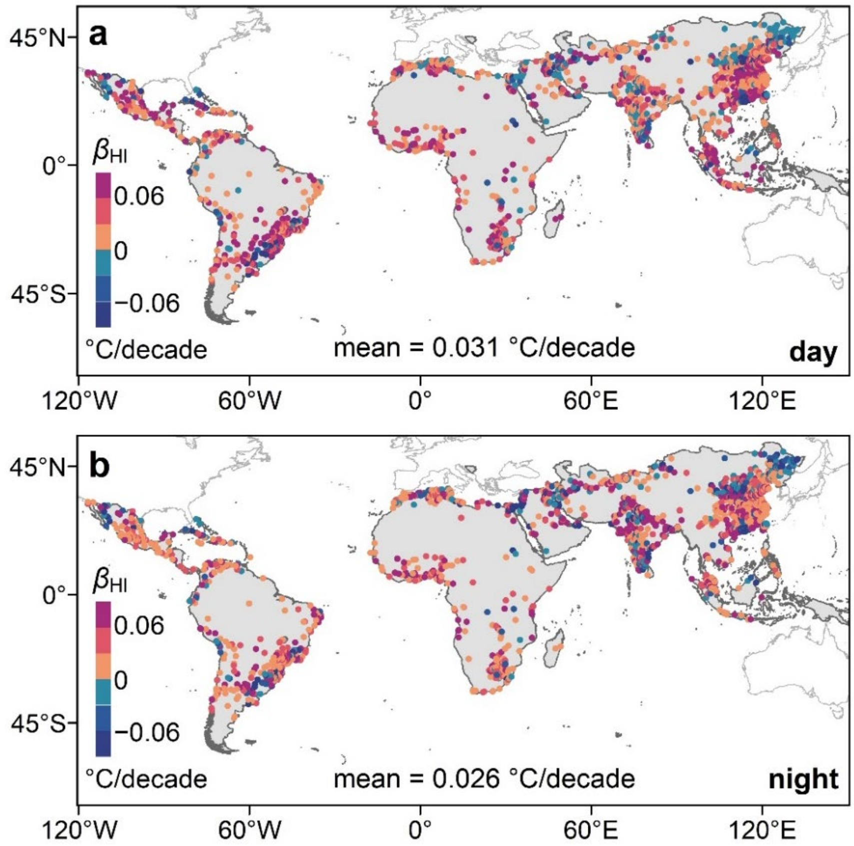

Fig. S26 | Spatiotemporal patterns of β_{HI} for urban transition zones across the Global South. (**a**) is for summer daytime and (**b**) is for summer nighttime.

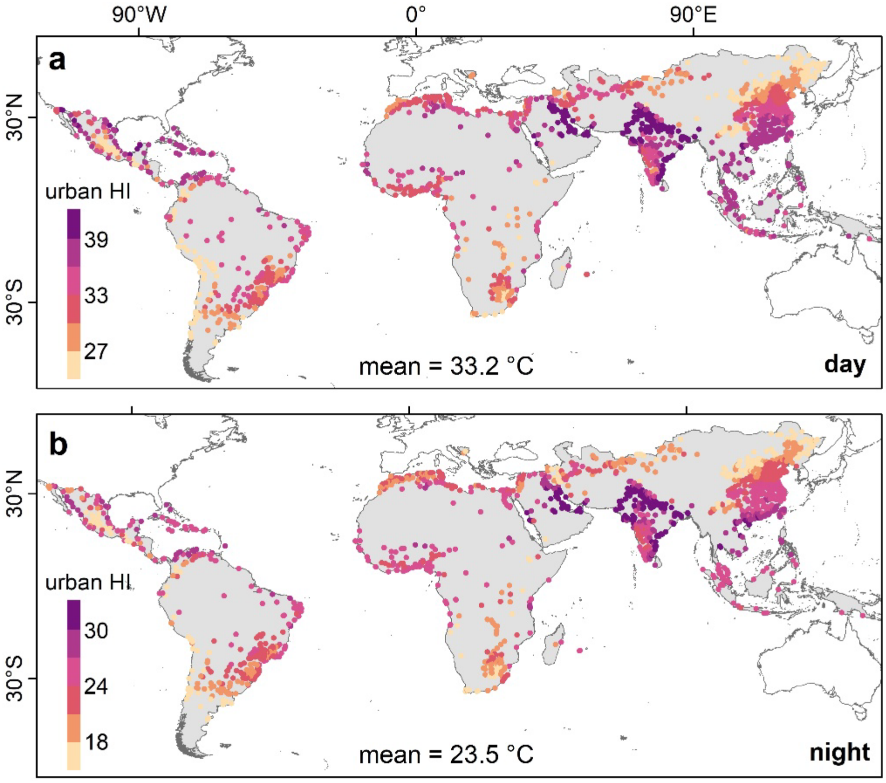

Fig. S27 | Spatiotemporal patterns of urban HI (averaged from 2003 to 2020) across Global South cities. (**a**) is for summer daytime and (**b**) is for summer nighttime.

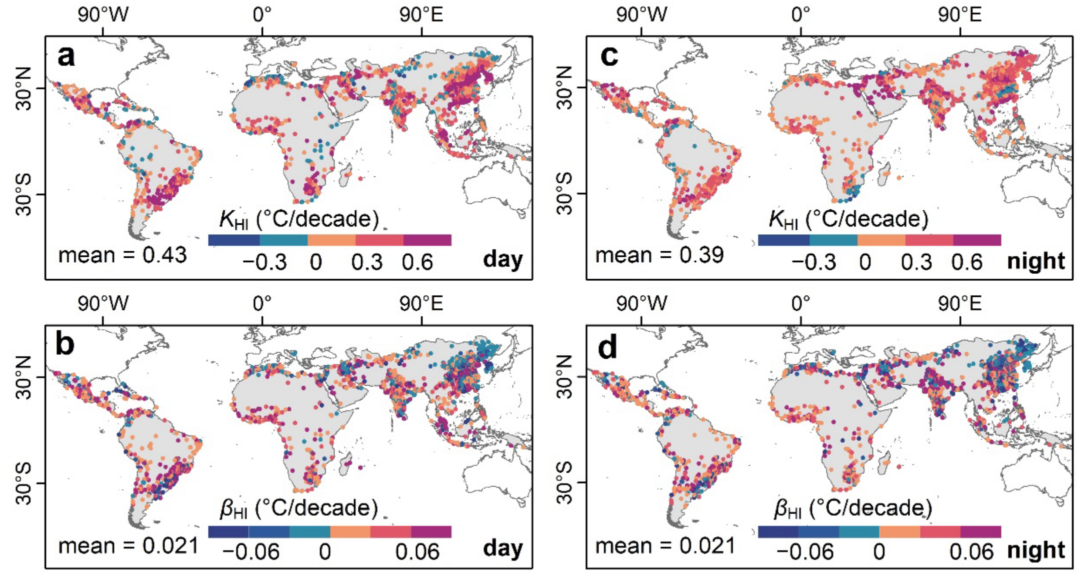

Fig. S28 | Potential impacts from urban HI estimation error on the quantification of K_{HI} and β_{HI}. Spatiotemporal patterns of K_{HI} and β_{HI} quantified based on the bias-perturbed 1-km resolution urban HI data, with (**a** and **b**) denoting the daytime case and (**c** and **d**) denoting the nighttime case.

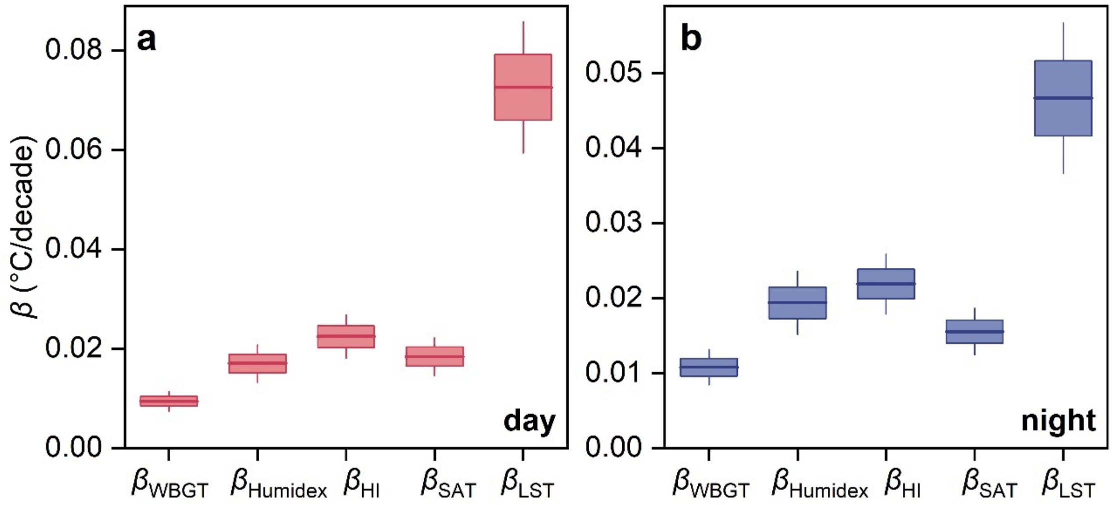

Fig. S29 | Statistical characteristics of urban browning-induced heat trends quantified using various temperature indices (i.e., $\boldsymbol{\beta}_{\mathbf{WBGT}}$, $\boldsymbol{\beta}_{\mathbf{Humidex}}$, $\boldsymbol{\beta}_{\mathbf{HI}}$, $\boldsymbol{\beta}_{\mathbf{SAT}}$, and $\boldsymbol{\beta}_{\mathbf{LST}}$). (**a**) is for daytime and (**b**) is for nighttime. The city sample sizes for β_{WBGT}, β_{Humidex}, β_{HI}, β_{SAT}, and β_{LST} during daytime are 2321, 2321, 2321, 2321, and 2326, respectively, whereas the nighttime sample sizes are 2261, 2261, 2261, 2261, and 2267, respectively. The center line represents the mean, while the lower and upper bounds of the whiskers indicate the 95% confidence interval.

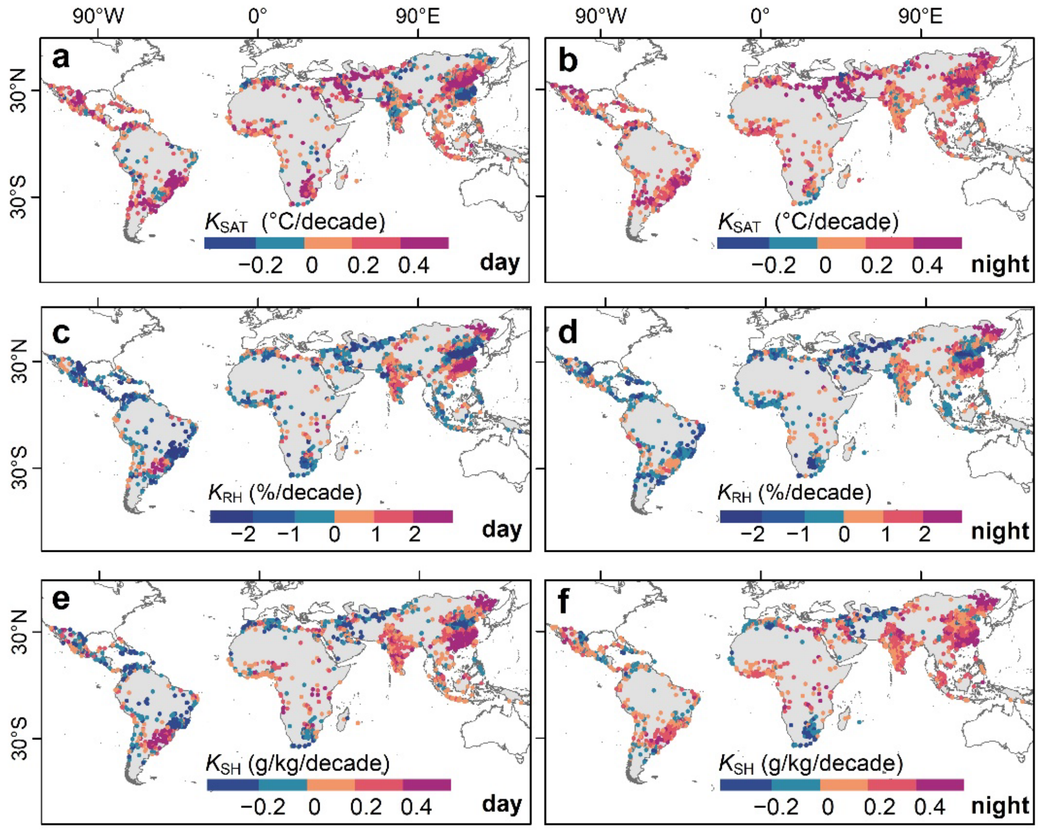

Fig. S30 | Spatiotemporal patterns of the trends in urban surface air temperature (K_{SAT}; a and b), relative humidity (K_{RH}; c and d), and specific humidity (K_{SH}; e and f) across Global South cities.

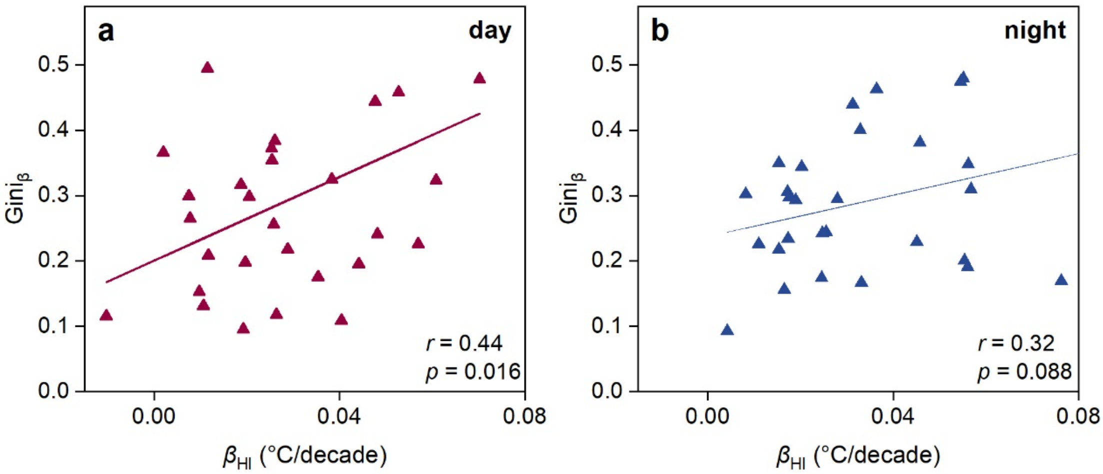

Fig. S31 | Statistical relationships between β_{HI} and its corresponding inequality (Gini$_\beta$) at the national scale. (**a**) is for daytime and (**b**) is for nighttime. The r and p values are obtained from a two-sided t-test with no adjustments.

C. Supplementary Tables

Table S1 | Country typologies depicting the relationships between K_{EVI} (decade^{-1}) and β_{HI} (°C/decade; physical perspective), with the thresholds defined using the mean values of K_{EVI} and β_{HI} across all Global South countries.

Thresholds	Country typologies
$K_{EVI} < -0.012$ and $\beta_{HI} > 0.030$	higher urban browning together with higher browning-induced heat stress amplification
$K_{EVI} < -0.012$ and $\beta_{HI} < 0.030$	higher urban browning yet with lower browning-induced heat stress amplification
$K_{EVI} > -0.012$ and $\beta_{HI} < 0.030$	lower urban browning together with lower browning-induced heat stress amplification
$K_{EVI} > -0.012$ and $\beta_{HI} < 0.030$	lower urban browning yet with higher browning-induced heat stress amplification

Table S2 | Country typologies depicting the relationships between urban HI (°C) and β_{HI} (°C/decade; physiological perspective), with the thresholds defined using the mean values of urban HI and β_{HI} across all Global South countries.

Thresholds	Country typologies
urban HI > 33.6 and β_{HI} > 0.030	higher heat risk together with higher browning-induced heat stress amplification
urban HI > 33.6 and β_{HI} < 0.030	higher heat risk together with lower browning-induced heat stress amplification
urban HI < 33.6 and β_{HI} < 0.030	lower heat risk together with lower browning-induced heat stress amplification
urban HI < 33.6 and β_{HI} > 0.030	lower heat risk together with higher browning-induced heat stress amplification

Table S3 | Country typologies depicting the relationships between economic growth (%) and β_{HI} (°C/decade; physiological perspective), with the thresholds defined using the mean values of economic growth and β_{HI} across all Global South countries.

Thresholds	Country typologies
economic growth > 59% and $\beta_{HI} > 0.030$	higher economic growth together with higher browning-induced heat stress amplification
economic growth > 59% and $\beta_{HI} < 0.030$	higher economic growth yet with lower browning-induced heat stress amplification
economic growth < 59% and $\beta_{HI} < 0.030$	lower economic growth together with lower browning-induced heat stress amplification
economic growth < 59% and $\beta_{HI} > 0.030$	lower economic growth yet with higher browning-induced heat stress amplification

D. Supplementary References

1. Gong, P. et al. Annual maps of global artificial impervious area (GAIA) between 1985 and 2018. *Remote Sens. Environ.* **236**, 111510 (2020).
2. Ren, G. Y. et al. Urbanization effects on observed surface air temperature trends in North China. *J. Clim.* **21**, 1333-1348 (2008).
3. Buizza, R., Milleer, M. & Palmer, T. N. Stochastic representation of model uncertainties in the ECMWF ensemble prediction system. *Q. J. R. Meteorol. Soc.* **125**, 2887-2908 (1999).
4. Pugachev, V. S. Probability theory and mathematical statistics for engineers. Elsevier (2014).
5. Ye, X. M., Xiao, X. B., Shi, J. B. & Ling, M. The new concepts of measurement error theory. *Measurement* **83**, 96-105 (2016).
6. IPCC *Climate Change 2022: Impacts, Adaptation, and Vulnerability* (eds Pörtner, H.-O. et al.) (Cambridge Univ. Press, 2022).
7. Rohde, R. et al. Berkeley earth temperature averaging process. *Geoinformatics Geostatistics An Overview* **1**, 1-13 (2013).
8. He, C. et al. The inequality labor loss risk from future urban warming and adaptation strategies. *Nat. Commun.* **13**, 3847 (2022).
9. Chakraborty, T. C., Venter, Z. S., Qian, Y. & Lee, X. H. Lower urban humidity moderates outdoor heat stress. *AGU Advances* **3**, e2022AV000729 (2022).
10. Chakraborty, T. C., Newman, A. J., Qian, Y., Hsu, A. & Sheriff, G. Residential segregation and outdoor urban moist heat stress disparities in the United States. *One Earth* **6**, 738-750 (2023).
11. Luo, M. & Lau, N. C. Increasing human-perceived heat stress risks exacerbated by urbanization in China: A comparative study based on multiple metrics. *Earth's*

Future **9**, e2020EF001848 (2021).

12. Masterton, J. M. & Richardson, F. Humidex: a method of quantifying human discomfort due to excessive heat and humidity. Environment Canada, Atmospheric Environment (1979).
13. Sherwood, S. C. How important is humidity in heat stress? *J. Geophys. Res.-Atmos.* **123**, 11808-11810 (2018).
14. Simpson, C. H., Brousse, O., Ebi, K. L. & Heaviside, C. Commonly used indices disagree about the effect of moisture on heat stress. *npj Clim. Atmos. Sci.* **6**, 78 (2023).
15. Zamanian, Z., Sedaghat, Z., Hemehrezaee, M. & Khajehnasiri, F. Evaluation of environmental heat stress on physiological parameters. *J. Environ. Health Sci. Eng* **15**, 1-8 (2017).
16. Chakraborty, T. C. et al. Urban versus lake impacts on heat stress and its disparities in a shoreline city. *GeoHealth* **7**, e2023GH000869 (2023).
17. Tuholske, C. et al. Global urban population exposure to extreme heat. *Proc. Natl. Acad. Sci. U. S. A*. **118**, e2024792118 (2021).
18. Chen, B. et al. Contrasting inequality in human exposure to greenspace between cities of Global North and Global South. *Nat. Commun.* **13**, 4636 (2022).
19. Wu, S. B., Chen, B., Webster, C., Xu, B. & Gong, P. Improved human greenspace exposure equality during 21st century urbanization. *Nat. Commun.* **14**, 6460 (2023).
20. National Oceanic and Atmospheric Administration. What is the heat index? (2012). https://www.weather.gov/ama/heatindex (accessed on 11 April 2024).
21. Houghton, J. Global Warming: The Complete Briefing. Cambridge University Press: the fifth Edition (2015).

22. Zhang, K. E. et al. Increased heat risk in wet climate induced by urban humid heat. *Nature* **617**, 738-742 (2023).
23. Ministry of Housing and Urban-Rural Development of the People's Republic of China (2004). https://www.mohurd.gov.cn/gongkai/zhengce/zhengcefilelib/200412/20041210_157113.html (accessed on 11 April 2024).
24. Zhang, Y. J., Zhang, T. Z., Zeng, Y. X., Cheng, B. D. & Li, H. X. Designating National Forest Cities in China: Does the policy improve the urban living environment? *Forest Policy Econ.* **125**, 102400 (2021).
25. Nguyen, T. T. et al. Implementation of a specific urban water management-Sponge City. *Sci. Total Environ.* **652**, 147-162 (2019).
26. Ministry of Housing and Urban-Rural Development of the People's Republic of China (2016). https://www.mohurd.gov.cn/gongkai/zhengce/zhengcefilelib/201601/20160129_226498.html (accessed on 11 April 2024).
27. Town and Country Planning Organisation. Urban greening guideline. Government of India Ministry of Urban Development (2014). http://tcpo.gov.in/urban-greening-guidelines-2014 (accessed on 11 April 2024).
28. Imam, A. U. & Banerjee, U. K. Urbanisation and greening of Indian cities: Problems, practices, and policies. *Ambio* **45**, 442-457 (2016).
29. Massaro, E. et al. Spatially-optimized urban greening for reduction of population exposure to land surface temperature extremes. *Nat. Commun.* **14**, 2903 (2023).
30. Jha, R. K., Nölke, N., Diwakara, B., Tewari, V. & Kleinn, C. Differences in tree species diversity along the rural-urban gradient in Bengaluru, India. *Urban For. Urban Green.* **46**, 126464 (2019).

31. Wolch, J. R., Byrne, J. & Newell, J. P. Urban green space, public health, and environmental justice: The challenge of making cities 'just green enough'. *Landsc. Urban Plan.* **125**, 234-244 (2014).

32. Dong, J., Guo, R. N., Guo, F., Guo, X. M. & Zhang, Z. Pocket parks-A systematic literature review. *Environ. Res. Lett.* **18**, 083003 (2023).

33. Lin, P. Y., Lau, S. S. Y., Qin, H. & Gou, Z. H. Effects of urban planning indicators on urban heat island: a case study of pocket parks in high-rise high-density environment. *Landsc. Urban Plan.* **168**, 48-60 (2017).

34. Wong, N. H., Tan, C. L., Kolokotsa, D. D. & Takebayashi, H. Greenery as a mitigation and adaptation strategy to urban heat. *Nat. Rev. Earth Environ.* **2**, 166-181 (2021).

35. Haaland, C. & van Den Bosch, C. K. Challenges and strategies for urban green-space planning in cities undergoing densification: A review. *Urban For. Urban Green.* **14**, 760-771 (2015).

36. Rosenzweig, C., Solecki, W. D., Hammer, S. A. & Mehrotra, S. Climate change and cities: First assessment report of the urban climate change research network. Cambridge University Press (2011).

37. C40 Cities. Rio de Janeiro Green Infrastructure Strategy. C40 Cities Climate Leadership Group (2017a). Retrieved from https://www.c40.org/cities/rio-de-janeiro

38. C40 Cities. Johannesburg's Green Strategy Implementation. C40 Cities Climate Leadership Group (2017b). Retrieved from https://www.c40.org/cities/johannesburg

39. Li, L. et al. Divergent urbanization-induced impacts on global surface urban heat island trends since 1980s. *Remote Sens. Environ.* **295**, 113650 (2023).

40. Wu, S. B. et al. Satellite observations reveal a decreasing albedo trend of global cities over the past 35 years. *Remote Sens. Environ.* **303**, 114003 (2024).
41. Li, L. et al. Competition between biogeochemical drivers and land-cover changes determines urban greening or browning. *Remote Sens. Environ.* **287**, 113481 (2023).
42. Meng, L. et al. Urban warming advances spring phenology but reduces the response of phenology to temperature in the conterminous United States. *Proc. Natl. Acad. Sci. U. S. A.* **117**, 4228-4233 (2020).
43. Hardwick, S. R. et al. The relationship between leaf area index and microclimate in tropical forest and oil palm plantation: Forest disturbance drives changes in microclimate. *Agric. For. Meteorol.* **201**, 187-195 (2015).
44. He, J. Y. et al. Recent advances and challenges in monitoring and modeling of disturbances in tropical moist forests. *Front. Remote Sens.* **5**, 1332728 (2024).
45. Koh, L. P. & Wilcove, D. S. Is oil palm agriculture really destroying tropical biodiversity? *Conserv. Lett.* **1**, 60-64 (2008).
46. Xu, Y. D. et al. Recent expansion of oil palm plantations into carbon-rich forests. *Nat. Sustain.* **5**, 574-577 (2022).